Acta Biomaterialia 110 (2020) 266–279

Contents lists available at ScienceDirect

Acta Biomaterialia

journal homepage: www.elsevier.com/locate/actbio

Full length article

A multifaceted biomimetic interface to improve the longevity of orthopedic implants

Michiel Croes[a,1], Behnam Akhavan[b,c,1,*], Omid Sharifahmadian[c], Haiyang Fan[d], Raya Mertens[d], Richard P. Tan[e,f], Aliza Chunara[b,c], Arifah A. Fadzil[b,c], Steven G. Wise[e,f], Moyo C. Kruyt[a], Sebastiaan Wijdicks[a], Wim E. Hennink[g], Marcela M.M. Bilek[b,c,f,h], Saber Amin Yavari[a]

[a] Department of Orthopedics, University Medical Center Utrecht, Utrecht 3508GA, the Netherlands
[b] School of Biomedical Engineering, University of Sydney, Sydney, NSW 2006, Australia
[c] School of Physics, University of Sydney, Sydney, New South Wales 2006, Australia
[d] PMA, Department of Mechanical Engineering, KU Leuven & Member of Flanders Make, Celestijnenlaan 300, Leuven B-3001, Belgium
[e] School of Medical Sciences, Dept of Phsyiology, University of Sydney, NSW 2006, Australia
[f] Charles Perkins Centre, University of Sydney, Sydney, New South Wales 2006, Australia
[g] Department of Pharmaceutics, Utrecht Institute for Pharmaceutical Sciences (UIPS), Utrecht University, Utrecht 3512JE, the Netherlands
[h] Sydney Nano Institute, University of Sydney, Sydney, New South Wales 2006, Australia

ARTICLE INFO

Article history:
Received 18 February 2020
Revised 23 March 2020
Accepted 9 April 2020
Available online 25 April 2020

Keywords:
Multi-functional biomaterials
Metal 3D printing
Plasma polymer films
Bone morphogenetic proteins
Bone integration
Scaffolds

ABSTRACT

The rise of additive manufacturing has provided a paradigm shift in the fabrication of precise, patient-specific implants that replicate the physical properties of native bone. However, eliciting an optimal biological response from such materials for rapid bone integration remains a challenge. Here we propose for the first time a one-step ion-assisted plasma polymerization process to create bio-functional 3D printed titanium (Ti) implants that offer rapid bone integration. Using selective laser melting, porous Ti implants with enhanced bone-mimicking mechanical properties were fabricated. The implants were functionalized uniformly with a highly reactive, radical-rich polymeric coating generated using a unique combination of plasma polymerization and plasma immersion ion implantation. We demonstrated the performance of such activated Ti implants with a focus on the coating's homogeneity, stability, and biological functionality. It was shown that the optimized coating was highly robust and possessed superb physicochemical stability in a corrosive physiological solution. The plasma activated coating was cytocompatible and non-immunogenic; and through its high reactivity, it allowed for easy, one-step covalent immobilization of functional biomolecules in the absence of solvents or chemicals. The activated Ti implants bio-functionalized with bone morphogenetic protein 2 (BMP-2) showed a reduced protein desorption and a more sustained osteoblast response both *in vitro* and *in vivo* compared to implants modified through conventional physisorption of BMP-2. The versatile new approach presented here will enable the development of bio-functionalized additively manufactured implants that are patient-specific and offer improved integration with host tissue.

Statement of Significance

Additive manufacturing has revolutionized the fabrication of patient-specific orthopedic implants. Although such 3D printed implants can show desirable mechanical and mass transport properties, they often require surface bio-functionalities to enable control over the biological response. Surface covalent immobilization of bioactive molecules is a viable approach to achieve this. Here we report the development of additively manufactured titanium implants that precisely replicate the physical properties of

* Corresponding author at: School of Biomedical Engineering, University of Sydney, Sydney, NSW 2006, Australia.
E-mail address: behnam.akhavan@sydney.edu.au (B. Akhavan).
[1] These authors contributed equally

https://doi.org/10.1016/j.actbio.2020.04.020

native bone and are bio-functionalized in a simple, reagent-free step. Our results show that covalent attachment of bone-related growth factors through ion-assisted plasma polymerized interlayers circumvents their desorption in physiological solution and significantly improves the bone induction by the implants both *in vitro* and *in vivo*.

1. Introduction

The choice for current metallic implants such as titanium (Ti), stainless steel, and cobalt chromium is based on their high resistance to mechanical stress and corrosion [1], while their bio-inert nature circumvents possible toxicity and undesired immune/foreign body responses [2]. However, in addition to the possibility of metal wear particle release causing gradual implant loosening [3], the poor bone-mimicking properties of current metallic implants do not facilitate rapid tissue surface bonding and physiologically relevant cellular interactions required for optimal integration with bone [4]. Consequently, the gradual loosening of metallic implants and a loss of biomechanical support remains the most significant factor limiting their longevity [5]. To illustrate, approximately 25% of all prosthetic implants exhibit loosening even in the absence of infection (aseptic loosening) during their lifetime [6]. The revision surgery needed to correct the aseptic failure is associated with a longer hospital stay, higher cost of treatment, and increased chance of complications as compared to the primary surgery, making it a huge socioeconomic burden [7]. The inadequate performance of metallic implants imposes an even bigger challenge when complex-shaped and porous metallic implants are clinically used as bone replacement materials [8,9]; that is, where substantial bone ingrowth is required and implant loosening must be avoided.

The current progress in additive manufacturing (AM) techniques provides an unprecedented opportunity to produce implants with a unique combination of mechanical [10], physical [11] and patient-specific [12] properties. For example, metallic 3D-printed implants with great potential as improved bioactive implants due to their ability to promote and sustain tissue ingrowth at the bone-implant interface have emerged in recent years [8]. In particular, porous titanium structures, that mimic the bone architecture and mechanical properties, are known to promote bone ingrowth [13,14]. Moreover, their Young's modulus can be precisely adjusted through rational designs to optimize the load transfer at the bone-implant interface and to reduce stress-shielding and bone resorption, providing better long-term bone bonding [9,15]. Additionally, the fully-interconnected porous structures of these implants have shown to provide the "guided" bone formation required to serve as bone substitute materials [8,9,16].

An ideal orthopedic implant not only supports enhanced bone ingrowth (osteoconduction), but also promotes rapid cell overgrowth by uncommitted progenitor cells and their osteogenic differentiation (osteoinduction) [4,17]. Although porous structures provide a powerful general platform for the design of tunable implants with improved long-term bone integration, they still do not possess the intrinsic surface functionalities to direct the crucial cell osteogenic functions in the early post-operative stage. The incorporation of bone-inductive growth factors, peptides, inorganic nanoparticles, chemokines and other biomolecules [4], not only supports the initial rigid fixation, but also favors the attachment of host cells to the material surface in "the race for the surface" against microbial colonization and biofilm formation [18,19].

Biomolecule surface functionalization of metallic surfaces has been most often carried out through physical adsorption [20,21]. However, for most clinical applications, physical adsorption is inappropriate, because non-covalently attached biomolecules are susceptible to desorption or competitive replacement by other molecules *in vivo* [20,22–24]. Because the bioactivity of a given biomolecule depends on its local concentration rather than on the overall dose applied, desorption of surface adsorbed therapeutic proteins leads to inefficient treatment in terms of cost effectiveness, clinical outcomes and side effects [25,26]. To illustrate, even though the bone morphogenetic protein (BMP)−2 growth factor is the single most potent bone-inductive factor identified to date, its widespread clinical use has been hampered. Its conventional application method, that is adsorption to a collagen scaffold, results in its desorption and leakage into surrounding tissue, hence a supraphysiologic dosage of protein is needed for efficacy *in vivo* [27]. This in turn raises concerns about high treatment costs [25] and potentially severe complications such as abnormal bone growth outside of the intended site [28,29].

Covalent immobilization onto a biomaterial surface offers localized, controlled and cost-effective use of clinically-applied therapeutic proteins and other macromolecular therapeutics. Covalent attachment through chemical linkers is an effective approach, but the chemistry involved usually demands a complex and cumbersome multi-step process, the success of attachment is dependent on the chemical nature of the substrate and biomolecule, and undesirable residual chemical compounds may be retained [20,30,31]. Plasma polymerization is a simple, alternative surface functionalization approach to wet-chemistry methods for the deposition of nano- to micrometer-thick polymer films on almost any solid material regardless of its shape, chemistry and geometry. This dry, environmentally friendly process is carried out at room temperature and produces almost zero waste [20,32]. Ion-assisted plasma polymerization (IAPP), in particular, offers the formation of highly robust polymeric films that contain a high concentration of radicals [33,34]. IAPP films are fabricated using a combination of plasma polymerization and plasma immersion ion implantation where the substrate is negatively biased in a pulsed manner during the deposition process [35,36]. This combination allows for enhanced ion bombardment during the film growth, thus increasing both the film-substrate adhesion and the concentration of radicals within the film structure.

The reactive radicals embedded in the coating gradually migrate to the surface from reservoirs beneath and facilitate direct covalent attachment of biomolecules through reactions with amino acid side chains [37]. This strategy allows for the immobilization of a wide range of bioactive molecules such as peptides [33,34] and proteins [38] that come into contact with the surface. Another important advantage of this technology is that this mechanism of biomolecule immobilization permits control of the density and orientation of molecules on the surface by simply applying an external electric field and/or tuning the solution pH [34].

Here, for the first time, we apply IAPP technology to produce biomimetic porous implants that show strong physical and chemical stability in biological media. This strategy addresses the clinical need of orthopedic implants that better resemble the native bone structure for improved long-term integration, but at the same time promote the rapid overgrowth by bone (progenitor) cells to provide rigid fixation. The first aim of this study was to design and validate the bone-mimicking mechanical and structural properties

Table 1
Parameters used for porous Ti implant design.

Design name	Mathematical equation	Solid volume fraction (%)	Wall/strut thickness (μm)	Wall/strut distance (μm)
Diamond	sin(x). sin(y). sin(z) + sin(x). cos(y) . cos(z) + cos (x) sin(y). sin(z) + cos(x) sin(y). cos(z) + cos(x) cos(y). sin(z) = 0.48	27	570	1150
Cell gyroid	sin(x). cos(y) + sin(y). cos(z) + sin(z). cos(x) = 0.65	27	790	1600
Sheet gyroid	sin(x). cos(y) + sin(y). cos(z) + sin(z). cos(x) = 0	27	370	1500

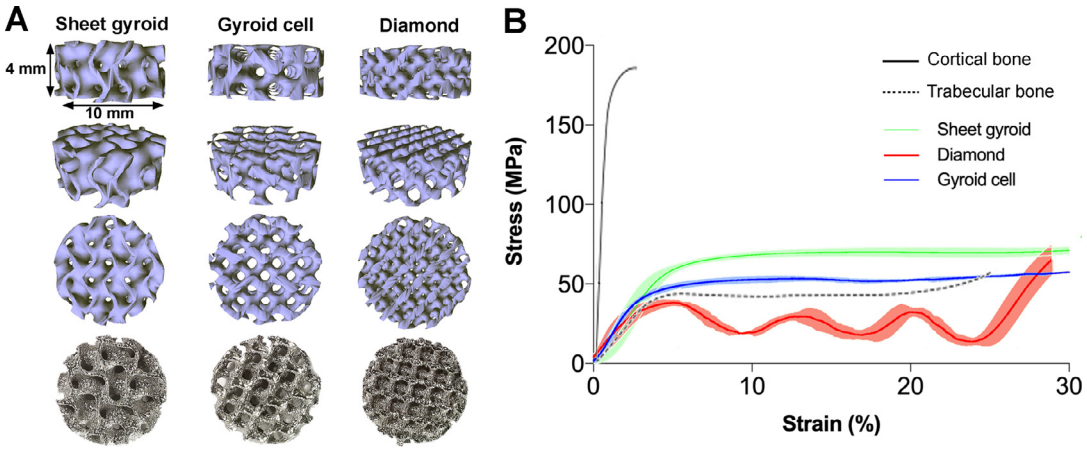

Fig. 1. Porous implant design and mechanical properties. (a) Images of the generated 3D surfaces and the fabricated implants according to the sheet gyroid, gyroid cell and diamond designs. (b) Average compressive stress-strain curves (n = 5 samples) of different designs of Ti porous implants. The representative stress-strain curves of human bone were adapted from literature [50].

of porous Ti implants fabricated by rational design principles and additive manufacturing. The second aim was to demonstrate the effectiveness of the IAPP approach to functionalize the porous Ti implants through a highly reactive and robust polymeric interlayer suitable for immobilization of bioactive molecules. A comprehensive *in vitro* study was performed to investigate the homogeneity, reactivity, and stability of the IAPP surfaces. The third aim was to determine whether covalent biomolecule immobilization onto the implants through IAPP resulted in an improved osteogenic response as compared to physical biomolecule adsorption. The biocompatibility and bioactivity of the newly functionalized implants were investigated both *in vitro* and *in vivo*.

2. Materials and methods

2.1. Rational design and printing of porous TI implants

2.1.1. Design

We used three topological designs based on triply periodic minimal surfaces (TPMS) which have zero mean surface curvature to mimic the curvature of trabecular bone [39]. These highly biomimetic designs were developed based on the mathematical equations shown in Table 1. The surfaces of these designs were generated using a 3D surface generator program (K3DSurf, http://k3dsurf.sourceforge.net/), as seen in Fig. 1A. The surfaces were exported so as to be compatible with Magics software (materialize, Leuven, Belgium). Using Magics, thickness/volume was created and smoothened until porous structures were achieved. The final implants used for *in vitro* and *in vivo* experiments had a cylindrical porous geometry (diameter ≈ 10 mm and height ≈ 4 mm).

2.1.2. Selective laser melting (SLM)

The 3D files were sliced into 30 μm layers by materialize Magics software and used to build 3D metal components using the Selective Laser Melting (SLM) technique from commercially pure Ti powder (CP-Ti, grade 1, LPW Ltd, Widnes, UK) with a particle size range of 10 - 45 μm. The SLM was carried out using an Mlab cusing machine (Concept Laser, Lichtenfels, Germany) equipped with a 100 W continuous fiber laser with a wavelength of 1.06 μm. The spot size was 50 μm and the process was carried out under inert argon atmosphere, ensuring an oxygen concentration < 0.3%. For SLM, a laser power of 42 W and a scanning speed of 180 mm/s were used. The laser paths were specifically generated to only provide non-overlapping contours with hatch distances of 77 μm in order to create the most consistent scanning parameters.

2.1.3. Morphological characterization

The nominal porosity was measured through dry weighing of three Ti implants (diameter ≈ 10 mm, height ≈ 4 mm). The total porosity of each specimen, ϕ, was defined by measuring the apparent density, ρ_{app}, using the volume and weight of the specimens and the known density of solid Ti (i.e., ρ_{bulk} = 4510 kg/m^3) as ϕ=1- ρ_{app} / ρ_{bulk}. Micro-computed tomography (micro-CT; Quantum FX, PerkinElmer, Waltham, US) using a tube voltage of 90 kV, a tube current of 180 mA, and a field of view of 10 mm was also carried out to assess the porosity. Afterwards, the data were analysed using BoneJ plugin (version 1.4.3) in Fiji [39,40].

2.1.4. Mechanical characterization

Compression tests according to ISO 13314:2011 standard [41] were carried out to assess the mechanical properties of the printed implants. For this reason, Ti samples different than those for *in vitro* and *in vivo* tests were used, i.e. cubic in shape with dimensions of 17 × 17 × 17 mm. A universal Instron machine with a maximum load of 30 kN and a crosshead displacement speed of 0.5 mm/min was used. The experiments were repeated five times in order to give a reliable calculation for the quasi elastic gradient and first maximum compressive strength.

2.2. Ion-assisted plasma polymerization (IAPP)

2.2.1. IAPP procedure

IAPP deposition was carried out using a custom-made device as described in detail in our previous publications [33,35]. Ti implants were suspended in an RF plasma discharge, powered at 50 W with an OEM ENI radio frequency generator (frequency: 13.56 MHz), while they were electrically connected to a pulsed bias (RUP6, GBS-Electronik, Großerkmannsdor, Germany). A mixture of acetylene, argon and nitrogen with flow rates of 5, 15, and 10 standard cubic cm per min (sccm), respectively, was used as the precursor gas, and the working pressure was adjusted to 110 mTorr by adjusting the pumping speed. The base pressure was always lower than 5.0×10^{-2} mTorr. The bias voltages (V_b) with pulse width of 20 µs were applied at a frequency of 3 kHz, while gas flow rates, working pressure and RF power were kept constant.

Samples were initially cleaned with argon plasma (RF power: 75 W, duration: 10 min, Ar flow rate: 40 sccm, working pressure: ~ 70 mTorr, V_b: - 500 V). To elucidate the role of ion bombardment on the stability of IAPP coatings, bias voltages of 0, - 500 and −1000 V were applied, while the plasma power drawn from the RF source was kept constant at 50 W. The deposition time was adjusted to achieve a constant thickness of 30 ± 5 nm for all samples. Polished silicon wafer pieces (boron doped, p-type) were also coated together with the Ti implants for spectroscopic ellipsometry measurements. To evaluate the stability of the IAPP coatings, the coated Ti implants were incubated at 37 °C for two months in Tyrode's simulated body fluid (SBF) solution with a composition described previously [42].

2.2.2. Surface characterization

X-ray photoelectron spectroscopy (XPS) measurements were carried out using a SPECS FlexMode XPS system equipped with a monochromatic X-ray source operating at 10 kV and 20 mA and a hemispherical analyzer. Survey spectra were collected in the range 15 to 1000 eV with a pass energy of 30 eV and resolution of 0.5 eV, while high resolution C1s spectra were recorded at a pass energy of 20 eV and resolution of 0.1 eV. CasaXPS (Version 2.3.14) was used for spectra calibration, elemental composition calculation and curve fitting of C1s spectra. A variable angle M2000 V spectroscopic ellipsometer (JA Woollam, NE, USA) was used to measure the thickness and refractive index of the IAPP coatings deposited on silicon wafers. The ellipsometry device was equipped with an XLS-100 light source and control module (EC-400). Three angles of incidence (65°, 70°, and 75°) were used for measurements in the visible and near-UV spectral regions (wavelength range: 200 – 1000 nm, 5 nm steps). A Cauchy model was applied to fit the obtained data using WVAESE32 software (JA Woollam). The average values of thickness and refractive index (at 630 nm) obtained from at least 3 measurements per sample are reported. A Phenom XL Scanning Electron Microscope (PhenomWorld, Eindhoven, The Netherlands) was used in secondary electron (SE) mode to obtain images of IAPP-coated implants before and after incubation in SBF at 37 °C for two months. Images were obtained at a voltage of 15 kV. The working distance was 7 mm.

2.3. Covalent protein immobilization and its bioactivity

2.3.1. Protein loading and binding strength

For BMP-2 (Inductos®, Medtronic BioPharma B.V, Maastricht, the Netherlands) immobilization, bare and IAPP-coated implants were incubated in a BMP-2/MilliQ water solution for 24 h at 4 °C. The concentration of BMP-2 in the solution varied within the range of 1 – 75 µg/ml, as indicated in the figures. Control samples without BMP-2 were prepared by incubation in MilliQ water. Samples were washed 3 × 5 min with MilliQ water and air-dried overnight prior to experiments. The amount of BMP-2 deposited onto the disks was determined using the NanoOrange® Protein Quantification Kit (Invitrogen, Carlsbad, CA, USA), according to the manufacturer's instructions.

To determine the BMP-2 release profile, BMP-2 immobilized implants were submerged in 500 µl PBS in 48-well plates and incubated in a humidified incubator at 37 °C with 5% CO_2. The supernatant was collected at days 1, 5, 10, 20, 30, and 40 and stored at −80 °C. The supernatant was replaced with fresh PBS at each time point. The concentration of eluted BMP-2 in the release samples was measured using an enzyme-linked immunosorbent assay (ELISA) kit according to the manufacturer's protocol (BGK8C060, Peprotech Ltd., London, UK).

To further confirm the covalent attachment and to demonstrate the homogenous distribution of covalently attached biomolecules onto IAPP-coated implants, we used Alexa Fluor 594-conjugated IgG protein (8 µg/ml, Abcam, Cambridge, UK) as a model molecule. The implants were incubated in IgG/PBS solution for 1 h at room temperature. The samples were then individually transferred into 50 mL falcon tubes filled with 5% sodium dodecyl sulfate (SDS) in sterile MilliQ water and allowed to rotate for 4 h at room temperature to desorb non-covalently bound IgG from the implant surface. The samples were then imaged using an upright fluorescence microscope (Zeiss Z1, Oberkochen, Germany) using 5x objective tiles stitched together to visualize the fluorescence profile of the entire implants.

2.3.2. BMP-2 bioactivity testing

Samples were UV-sterilized on each side for 30 min (7 mW/cm^2) prior to the culture experiments. The bioactivity of the BMP-2 coating was measured using ATDC5 cells as a reporter cell line (ATCC, Manassas, VA, USA), as they produce high levels of alkaline phosphatase (ALP) upon BMP-2 stimulation [43]. ATDC5 culture medium consisted of DMEM/F12 (Gibco, Grand Island, NY) supplemented with 10% FBS (Hyclone, Thermo Scientific, Waltham, MA, USA) and 100 units/ml penicillin/streptomycin (Invitrogen, Carlsbad, CA, USA). The cells were seeded onto the implants at 2×10^5 cells in 500 µl medium in each well of a 48-well plate. After 72 h, the cells were lysed in 0.2% (v/v) Triton X-100/PBS for 15 min at room temperature. The ALP activity in the lysate was determined by conversion of the p-nitrophenyl phosphate liquid substrate system (Sigma, St. Louis, MO, USA), measured at 405 nm and corrected at 655 nm (Bio-Rad, Hercules, CA, USA). To normalize for the number of cells, the ALP activity was divided by the DNA content as measured by the Quant-It PicoGreen kit (Invitrogen), according to the manufacturer's instructions. The seeded implants were transferred to a new well plate before performing further analyses.

2.3.3. Cell cytocompatibility and osteoblast differentiation

The pro-inflammatory activity of the functionalized IAPP implants with or without BMP-2 was tested by measuring the induction of NF-κB/AP-1 activity in RAW-Blue macrophages (InvivoGen, San Diego, CA, USA). An excessive activity of NF-κB due to the IAPP surfaces should be ruled out, since this could lead to uncontrolled osteoclast activity and inflammation-associated bone loss around implants [44]. The cells were seeded at a density of 1×10^6 cells in 500 µl medium in a 48-well plate, using DMEM/F12 (Gibco) supplemented with 10% FBS (Hyclone) and 100 units/ml penicillin/streptomycin (Invitrogen). The supernatant was collected after 24 h and the AP-1 activity was measured according to the manufacturer's instructions. Implants pre-soaked in lipopolysaccharide (LPS, 1 µg/ml, L5418, Sigma) for 24 h were used as positive controls for NF-κB/AP-1 activity. The metabolic activity of the RAW-Blue macrophages after 24 h was measured using the AlamarBlue Cell

Viability Reagent (Thermo Scientific). Fluorescence was detected utilizing the Fluoroskan Ascent FL multiplate reader (Thermo Labsystems, Helsinki, Finland) after 2 h incubation with AlamarBlue reagent.

Human mesenchymal stem cells (MSCs) were seeded onto the implants to investigate cell attachment, proliferation, and differentiation. For MSC isolation, bone marrow was obtained from the calcaneus bone of an adolescent female undergoing orthopedic surgery (University Medical Center Utrecht, Utrecht, the Netherlands) after written informed consent and approval of the local medical ethical committee. The MSC isolation method, culture conditions and cell characteristics are described elsewhere [45]. Cells were seeded onto the discs at 2×10^5 cells in 500 µl medium in a 48-well plate and cultured in growth medium, consisting of α-MEM (Invitrogen) supplemented with 10% FBS (Hyclone), 100 units/ml penicillin/streptomycin (Invitrogen), and 0.2 mM L-ascorbic acid 2-phosphate (Sigma). The seeded implants were transferred into a new well plate before performing the analyses. To determine the bioactivity of covalently attached BMP-2 on MSCs, samples were treated with 5% (v/v) Tween-20/MilliQ for 2 h at 37 °C, and washed 3 × 5 min with MilliQ water, prior to MSC seeding.

The adherence and proliferation of MSCs on uncoated and functionalized implants were determined qualitatively using a live/dead cell viability kit, as described by the manufacturer (Molecular Probes, Thermo Scientific). Live (green) and dead cells (red) were imaged using a fluorescence microscope (IX53, Olympus, Tokyo, Japan). The MSC metabolic activity and DNA content were measured using aforementioned AlamarBlue and Picogreen assays, respectively.

The ALP activity normalized per DNA was measured as an early marker of osteoblast differentiation. MSCs were cultured in growth medium for a total of 5 days. The growth medium was refreshed on the third day of culture. The ALP activity and DNA content of MSCs lysed in 0.2% (v/v) Triton X-100/PBS were quantified using the same protocol used for the ATDC5 cells.

2.4. In vivo *subcutaneous implantation study*

2.4.1. Subcutaneous implantation model

The *in vivo* study was performed with approval of the local Ethics Committee for Animal Experimentation (Utrecht University, the Netherlands) and the Central Authority for Scientific Procedures on Animals (approved protocol no. AVD115002016445). Eight male Fisher rats (F344/IcoCrl, 16-week old, Charles River, L'Arbresle, France) were housed in groups at the Central Laboratory Animal Institute (Utrecht University). Food and water were available ad libitum.

Surgery was performed under anesthesia with 2 – 3% isoflurane. The animals were given Buprenorphine (0.03 mg/kg s.c.; Temgesic®, RB Pharmaceuticals Limited, Slough, UK) for pain relief once pre-operatively and for two days post-operatively, twice daily. After shaving and disinfecting the skin, subcutaneous pockets were created in the dorsum by incision of the skin and blunt dissection of the subcutaneous tissue. For the *in vivo* study, implants were used identical to those used for the *in vitro* study (diameter ≈ 10 mm and height ≈ 4 mm). The implants were allocated to one of the eight predefined subcutaneous implantation locations in the dorsum using an online randomizer tool. The animals received the conditions listed in Table 2, thus each animal received seven to eight implants (i.e. groups 1–2 implanted in half of the animals, groups 3–8 implanted in all animals). The skin was closed with resorbable sutures (Monocryl®, Ethicon, NJ, USA). The rats were euthanized with CO_2 after 8 weeks.

Table 2
Groups included in the rat study.

Group	Implant	BMP-2 [a] (µg/ml)	Number of samples per group
1	Ti	0	4
2	Ti/IAPP	0	4
3	Ti	5	8
4	Ti/IAPP	5	8
5	Ti	15	8
6	Ti/IAPP	15	8
7	Ti	75	8
8	Ti/IAPP	75	8

[a)] Concentration of solution used for immobilization.

2.4.2. Histological assessment

The explanted discs were fixed in 4% (w/v) formaldehyde, dehydrated in an ethanol series, and embedded in methyl methacrylate (MMA, Merck Millipore, MA, USA). The discs were completely sectioned with a diamond saw microtome (Leica, Nusslochh, Germany) with a blade thickness of 300 µm, resulting in 6–8 sections per sample. The 50 µm-thick sections were stained with basic fuchsin (0.3% in water) and methylene blue (1% in 0.1 M sodium borate, pH 8.5), both for 1 min. Each disk was scored for the presence of bone (i.e. bone incidence). In addition, the sections containing bone were pseudocoloured in Adobe Photoshop (Adobe Systems, San Jose, CA, USA) using a standardized method [46]. The bone volume is expressed as the percentage of bone tissue in the available pore space (i.e. bone area%). The mean bone area% is used when multiple sections from a disk contained bone.

2.5. Statistical analysis

All data are presented as the mean ± standard deviation. One-way ANOVA was performed to compare the means of the group in SPSS (v24, IBM, Armonk, NY). Single factor ANOVA was performed in Microsoft Office Excel (Professional Plus 2016) to compare the means of values reported for deposition rates and refractive indices. The Mann-Whitney U test was performed when there was no homogeneity of the variance. The significance of differences in bone incidence between groups was analyzed with a linear mixed-model approach with binary outcome measure (i.e. bone or no bone). The Pearson Chi-Square test was performed to test the possible association between the BMP-2 concentration and bone incidence. Bonferroni post-hoc corrections were applied for multiple comparisons.

3. Results and discussion

3.1. AM and mechanical properties of porous titanium

An ideal orthopedic implant should provide both bone osteoconduction and osteoinduction, optimally [4,17]. Considering the impaired osteogenic response in different clinical scenario's, such as in the case of patients with poor bone quality or compromised immune system [47], we followed a multifaceted approach in the design and bio-functionalization of a porous Ti implant to tackle the problem of aseptic loosening.

Mimicking the topology and curvature of trabecular bone to generate a zero mean surface curvature has been seriously considered as a prerequisite for tissue regeneration [48,49]. Therefore, three TPMS structures, namely sheet gyroid, gyroid cell and diamond, have been designed and fabricated for this study. As observed from Table 1, the sheet gyroid porous implant, for example, had a sheet thickness of ≈ 370 µm and a pore size (wall to wall distances) of ≈ 1500 µm. This resulted in a solid volume fraction of 27% (i.e., 73% open porosity) and a total surface area of about 5 times larger than that of an equally sized solid cylinder. As per

Table 3
Mechanical properties of the Ti designs.

Structure	First maximum compressive strength (MPa)	Quasi elastic gradient (MPa)
Sheet gyroid	69.4 ± 2.8	1713 ± 198
Gyroid cell	53.6 ± 1.4	1539 ± 35
Diamond	38.9 ± 1.8	1325 ± 304

AM, the SLM process produced porous structures whose morphological characteristics closely matched those of the CAD designs (Fig. 1A). Based on micro CT measurements, the relative density of the porous structure as well as the strut thickness and distance were within 10% of their designed values, verifying a successful application of the SLM process.

This porous implant allowed 1) a pore size exceeding 300 μm to enable cell migration, nutrition, and oxygenation, leading to enhanced tissue regeneration [51], 2) and an increased surface area to amplify the effects of surface bio-functionalization. Nevertheless, the mechanical compatibility of printed implants and bone plays a more significant role towards the development of an ideal implant. Thus, the bone-mimicking mechanical properties of different porous implants were investigated via the compression test (Fig. 1B). The sheet gyroid structure has only walls with no sharp nodes. Yang et al. showed that additively manufactured Ti scaffolds with this structure have zero surface curvatures [52]. Therefore, although the main deformation mechanism of the cells is bending [53], gyroid structure does not collapse by going through successive failure of the walls [54,55]. This can be an advantage of gyroid in comparison with more traditional structures such as diamond which may show a fluctuation in the compressive stress-strain curve [56]. This behavior is because sharp nodes and struts in diamond structure can cause successive failure and crush of the struts one after another, fluctuating the compressive stress-strain curve.

Accordingly, quasi-elastic gradients (as apparent stiffness of the porous implants) and the first maximum strengths (as the demonstration for mechanical strength) were measured according to the ISO 13314:2011 standard [41]. As shown in Table 3, amongst diamond, cell gyroid and sheet gyroid structures, the sheet gyroid structure demonstrated the highest mechanical performance with a quasi-elastic gradient of 1713 ± 198 MP and first maximum strength of 69.4 ± 2.8 MPa.

These mechanical properties favorably lie in between the properties of cortical and cancellous bone (Fig. 1B) [57]. Therefore, from a mechanical compatibility point of view, a sheet gyroid structure is the best candidate to replace the total bone structure. Further tests in this work were, therefore, only carried out using implants with a sheet gyroid structure.

3.2. Deposition of ion-assisted plasma polymer films

Following orthopedic implant placement, a rapid matrix production is required to minimize the micromotions of the implant relative to the bone and to reduce the possibility of implant rejection by means of fibrous capsule formation [58], This is particularly of relevance in patients that start their load-bearing activities on orthopedic implants relatively soon post-operation [47,59,60], or when they suffer an impaired osteogenic response [47,61].

To allow for the direct covalent attachment of bone-promoting biomolecules, we investigated the feasibility of creating a homogeneous and stable IAPP coating on the porous 3D-printed Ti implants. To achieve a homogenous IAPP layer all around and throughout the implants, a unique plasma polymerization configuration was employed, wherein the implants were suspended in the RF plasma while they were electrically connected to a bias voltage (V_b) source to enhance the ion bombardment during the film growth (Fig. 2A). As shown previously on 2D Ti surfaces [35], this strategy allows for a high flux of ionized species penetrating the surface, to enhance the interfacial adhesion strength between the coating and the Ti substrate and to create a high concentration of reactive radicals within the IAPP structure as it grows.

The role of the applied bias, V_b, in the production of homogenous and stable IAPP coatings on the Ti implants, was investigated. XPS surface chemical analyses showed the absence of Ti signals irrespective of the V_b (Fig. 2B), which indicates that the IAPP layers were all thicker than 8–10 nm, i.e. the sensitivity depth of XPS [62]. Moreover, ellipsometry measurements showed that a constant IAPP layer thickness of 30 ± 5 nm was achieved for all samples by adjusting the deposition time for various V_b values. The composition of carbon, oxygen and nitrogen elements in the IAPP layer depended on the applied V_b. When increasing the V_b from 0 to −1000 V, the carbon and oxygen atomic concentrations increased from 74.3% and 3.3% to 85.7% and 6.3%, respectively, while that of nitrogen decreased from 22.3% to 8.1% (Fig. 2B). The presence of oxygen in the coating structure, despite the fact that the precursor gas mixture ($Ar + C_2H_2 + N_2$) contained no oxygen, is explained by the 'autoxidation' processes initiated by carbon-centered radicals within the coatings [36]. The increasing oxygen atomic concentration as a function of V_b is due to the higher concentration of reactive radicals that are generated at higher bias ion bombardment conditions [63]. The inverse relationship seen for nitrogen, i.e. the decrease in its atomic concentration for increasing V_b, is most likely attributed to a preferential etching mechanism where more nitrogen-containing species are selectively ablated from the polymer structure with higher ion bombardment [35]. The diffusion of liberated nitrogen atoms is also increased under elevated ion bombardment conditions, facilitating the formation N_2 molecules that leave the coating and further contributing to the decrease of the nitrogen concentration.

To further elucidate the changes of IAPP surface chemistry as a function of V_b, three peaks - i.e. C1 ($C - C/C - H$ at binding energy (BE) ≅ 284.6 eV), C2 ($C - O/C - N$ at BE ≅ 286.5 eV), C3 ($C = O/N - C = O$ at BE ≅ 287.5 eV) - were fitted in the C1s high resolution spectra (Fig. 2C, 2D) [33,64]. For the highest V_b, the C1s spectrum showed a relative increase in C1 compounds and a decrease in C2 and C3 compounds (Fig. 2C). When closely examining the curves, the full-width at half maximum (FWHM) of the C1s peak was found to become progressively smaller when increasing the V_b, and the shoulder at higher binding energies became narrower (Fig. 2D). These changes further support the XPS survey elemental composition data and indicate that there is an increase in the concentration of carbon compounds in the neutral environment and a decrease in oxygen- and/or nitrogen-containing moieties. Considering that the oxygen atomic concentration is higher for samples deposited at higher V_b, it can be concluded that the reduced concentration of C2 and C3 compounds is primarily due to the decrease of nitrogen-containing moieties, a conclusion that agrees with lower nitrogen atomic concentration at greater applied V_b (Fig. 2B).

The deposition rate was decreased as a function of V_b (Fig. 2E), implying that the balance of polymerization and ablation processes shifts toward the ablation with enhanced ion bombardment, as regulated by the arrival of energetic ions at the surface. The refractive indices of the IAPP coatings were obtained to elucidate variations in the cross-linking degree of the IAPP coatings (Fig. 2F). There was a positive relationship between the applied V_b and the refractive index of the coatings, which indicates higher cross-linking and density at higher V_b [65]. This finding is explained by the higher fluxes of energetic ions arriving at the surface and thus increasing the fragmentation of deposited species that recombine to form highly cross-linked structures [66].

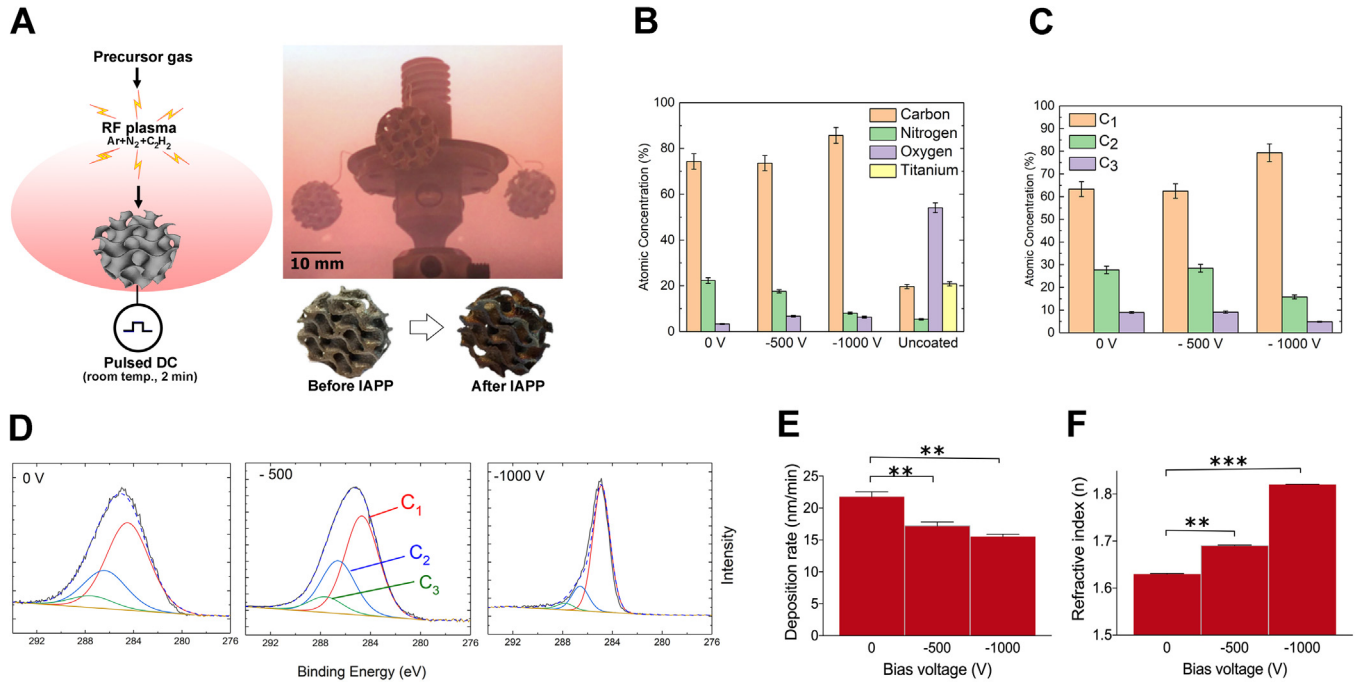

Fig. 2. Chemical and physical characterization of IAPP layers. (a) Illustration of the IAPP coating system. The sample holder is biased by a negative voltage during deposition. (b) XPS survey elemental composition of bare (uncoated) and IAPP-coated Ti implants. The IAPP coatings were deposited using various bias voltages as indicated. (c) Atomic concentrations of peak-fitted C1s components of the IAPP layers deposited at different bias voltages. (d) High resolution C1s spectra of IAPP coatings deposited on Ti implants at various bias voltages. (e, f) Deposition rate (e) and refractive index (f) of IAPP coatings prepared at various bias voltages. $^{**}p < 0.01$, $^{***}p < 0.0005$ (Single factor ANOVA). XPS error bars are calculated from the background noise.

3.3. Physico-chemical stability of IAPP coatings

The chemical and physical stability of coatings applied for biomedical implantable devices are of critical importance, particularly for bone implants where the coatings should resist failure at the interface from the moment of surgical insertion. To evaluate the robustness of the IAPP coating on Ti implants, we examined the surface chemistry by XPS and morphological changes by SEM following two months incubation in Tyrode's Simulated Body Fluid (SBF) at 37 °C.

Comparing the XPS elemental compositions after SBF incubation (Fig. 3A) with those of as-deposited samples (Fig. 2B) indicated that the greatest changes in surface chemistry, i.e. the uptake of oxygen and reduction of nitrogen concentration, occurred for the IAPP coating deposited in the absence of a V_b. This was consistent with the XPS high resolution C1s spectra (Fig. 3B) and the calculated area percentage of various carbon-containing components (Fig. 3C). These data show that the most pronounced changes in the concentrations of $C = O$ and $N–C = O$ groups after incubation in SBF solution occur for the sample deposited without V_b.

The SEM micrographs showed variations in IAPP coating stability depending on the applied V_b (Fig. 3D). The as-deposited IAPP coatings showed a feature-less surface, identical to the topography of the bare Ti implant. Confirming the XPS results that showed no Ti signals, none of the coatings were delaminated upon incubation in the SBF solution. However, the IAPP coatings deposited at a V_b of either 0 or −1000 V showed buckling features on the surface, whereas no signs of cracking or buckling were present for the coating deposited at – 500 V.

These data highlight the critical role of ion-bombardment in achieving both chemically and physically stable plasma polymer coatings on Ti implants. On one hand, we explain the greater stability of IAPP coatings deposited in the presence of an appropriate bias voltage by their higher physical integrity. The more densely cross-linked structure, shown by the improved refractive index values (Fig. 2F), may restrict the intrusion of O_2 and H_2O molecules to active radical sites, thus moderating the kinetics of oxidation and hydrolysis reactions [67]. In addition, under elevated ion bombardment conditions, a stronger interfacial adhesion is achieved between the IAPP coating and the Ti substrate due to the increased formation of metallic carbide and oxycarbide bonds at interface [42]. On the other hand, the increase of ion bombardment increases the residual stress in the plasma polymer films, which in turn negatively influences the long-term stability, e.g. by promoting the formation of buckling features. Following this line of reasoning, the superb physical stability of the IAPP coating prepared at a relatively mild ion-treatment condition ($V_b = -500$ V) can be explained by a balance achieved between the residual stress of the coating and the substrate-coating interfacial adhesion. Since the IAPP coating deposited at −500 V was the optimum for achieving the most stable coating, this condition was selected for the remainder of the experiments.

3.4. Homogeneity of IAPP coating deposited on TI implants

To evaluate whether the IAPP coating is deposited with a homogenous chemistry, we analyzed the chemistry of the 3D-printed implants at their top, side and bottom surfaces (schematically depicted in Fig. 4A). The XPS survey spectra (Fig. 4A) and the calculated elemental compositions (Fig. 4B) (C: 76.2 ± 0.7%, N: 17.1 ± 0.4%, O: 6.5 ± 0.5%), showed that the surface chemistry of the IAPP coating is identical all around the 3D Ti implants within the experimental errors. Furthermore, the absence of Ti signals in the survey spectra demonstrates that the thickness of the coating is at least 8 nm for different investigated locations. The C1s high resolution spectra (Fig. 4C) and the area percentage of carbon-containing components (Fig. 4D) were also identical within the XPS measurement errors for the three analyzed locations. Altogether, these results demonstrate that suspending porous metallic implants in an RF plasma, while being connected to a V_b source,

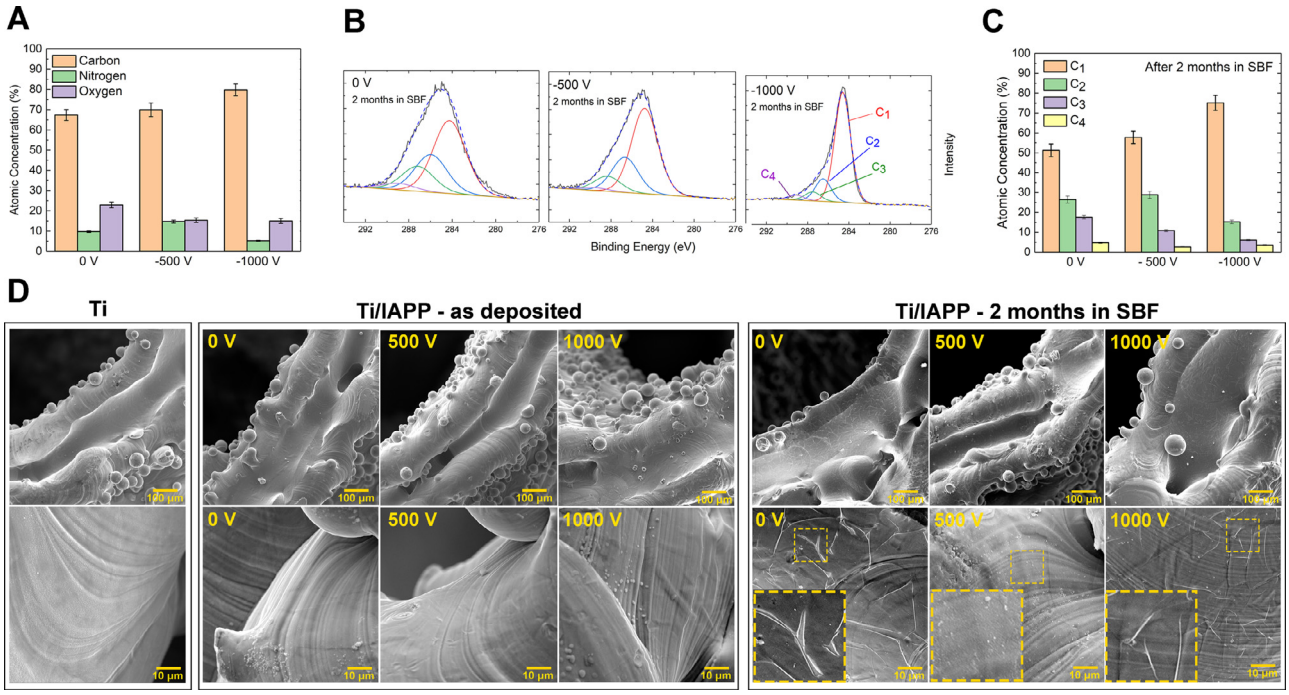

Fig. 3. Long-term stability of the IAPP layer. (a) XPS survey elemental composition after IAPP coating and incubation in Tyrode's SBF at 37 °C for two months. (b, c) High resolution C1s spectra (b) and atomic concentrations of peak-fitted C1s components (c) of IAPP-coated Ti implants after incubation in Tyrode's SBF at 37 °C for two months. (d) SEM images of bare Ti and IAPP-coated Ti implants prepared at various bias voltages before and after incubation in Tyrode's SBF. The insets in the right figure panel show the buckling of the IAPP coating at bias voltages of 0 and −1000 V. XPS error bars are calculated from the background noise.

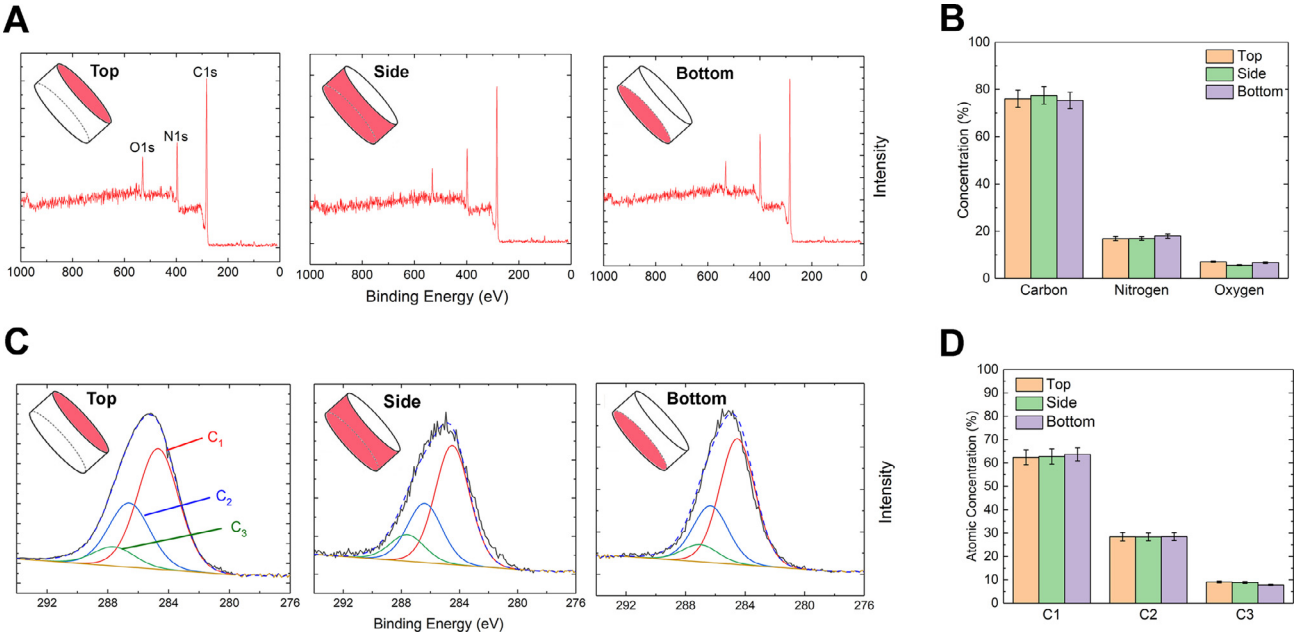

Fig. 4. Homogeneity of IAPP coating around the Ti implant. (a, b) Survey spectra (a) and calculated elemental composition (b) of XPS data recorded from the top, side and bottom surfaces of IAPP-coated Ti implants. (c, d) High resolution C1s spectra (c) and atomic concentrations of peak-fitted C1s components (d) for the top, side and bottom surfaces of IAPP-coated Ti implants. XPS error bars are calculated from the background noise.

is an effective approach to achieve chemically homogenous deposition of IAPP coatings all around the current optimized porous design.

3.5. Covalent protein immobilization

We used fluorescently-labeled IgG as a model molecule to visualize the homogeneity of plasma polymerized coatings deposited on Ti implants. Detergents like SDS and Tween-20 remove proteins physisorbed on Ti, but are not able to detach covalently bound proteins [68,69]. Homogenous presence of fluorescently-labeled IgG covalently attached to the IAPP interlayer was confirmed by showing its resistance to SDS washing in the Ti/IAPP group, whereas removal of most physically adsorbed IgG from Ti surfaces was evident (Fig. 5A).

Further in-depth investigations of the covalent attachment and bioactivity of biomolecules immobilized onto the IAPP surfaces were performed using BMP-2. BMP-2 was chosen as a model pro-

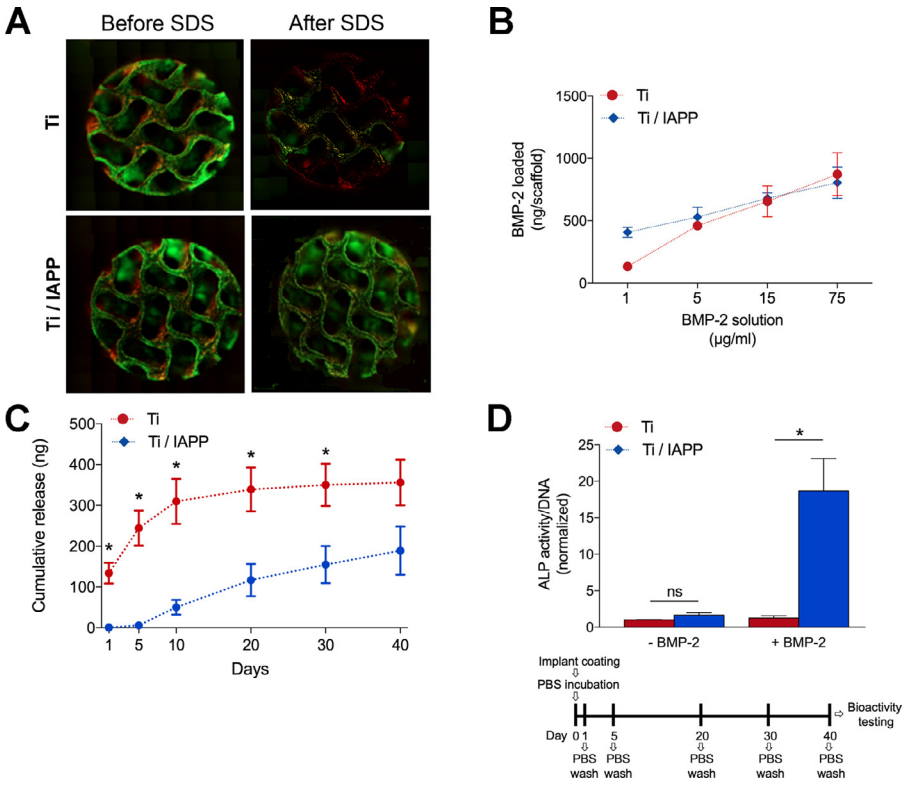

Fig. 5. Covalent protein immobilization through the IAPP film interlayer. (a) Ti and Ti/IAPP implants were incubated in FITC-conjugated IgG protein solution for 24 h. Samples were washed with SDS detergent to desorb physically-adsorbed proteins. Fluorescence imaging was performed before and after the washing step to show covalent attachment of the immobilized protein (green). (b) Protein quantification of total surface-bound BMP-2 after 24 h as a function of BMP-2 concentration in the immobilization solution. (c) Cumulative BMP-2 release profile following BMP-2 immobilization (15 µg/ml) for 24 h on Ti and Ti/IAPP implants as measured by ELISA. (d) BMP-2 bioactivity measured after 40 days incubation of implants in PBS. The ALP activity/DNA was measured in ATDC5 reporter cultured on bare or IAPP-functionalized Ti implants, either or not immobilized with BMP-2 (15 µg/ml). Data are represented as the mean ± SD ($n = 3$). *$p < 0.05$ (Mann-Whitney U).

tein because of its clinical relevance [28], and since its physical adsorption to Ti surfaces can lead to its rapid desorption and/or changes in protein activity [70,71], opting for covalent immobilization methods.

A titration experiment was performed to determine the loading efficiency of BMP-2 (1 – 75 µg/ml) onto Ti and Ti/IAPP implants. Measurements using a protein quantitation kit showed that a similar amount of BMP-2 was initially loaded onto Ti and Ti/IAPP implants (Fig. 5B). After incubation of the coated implants in PBS, the release profile showed a plateau in BMP-2 release between days 5 and 10 for Ti implants, whereas a plateau in BMP-2 release was not reached even after 40 days for Ti/IAPP implants (Fig. 5C). The prolonged functionality of the BMP-2 coating was confirmed using ATDC5 reporter cells, showing bioactivity of the IAPP+BMP-2-functionalized implants even after 40 days incubation in PBS and multiple washes (Fig. 5D). These data show that the specific interaction of BMP-2 with the IAPP interlayer resulted into its long-lasting immobilization, in contrast to the physisorbed BMP-2.

3.6. Human mesenchymal stem cell (MSC) cytocompatibility and differentiation

The bone coverage of orthopedic implants requires the recruitment of potential osteogenic cell populations, and their differentiation into mature matrix-producing osteoblasts [72,73]. Therefore, human MSCs were used as a relevant cell source to evaluate whether the functionalized implants provide the required cytocompatibility for cell adhesion, expansion and osteogenic differentiation. As shown by live/dead staining, the IAPP films supported the adhesion and spreading of MSCs equally to bare Ti implants, and non-viable cells were only scarcely observed (Fig. 6A, 6B). The higher MSC metabolic activity (Fig. 6C) and DNA content (Fig. 6D) in the Ti/IAPP group, as compared to the bare Ti group, indicated that the IAPP film enhanced the proliferation of the MSCs after their initial attachment. These results show the cytocompatibility of the Ti/IAPP interface towards human MSCs, which could be explained by the attachment of growth and adhesion factors present in the serum or other cell culture medium components to the IAPP surface.

Subsequent BMP-2 immobilization resulted in various morphological cell changes, indicating enhanced cell differentiation. These changes were most obvious for the IAPP-functionalized implants. After five days, the formation of a confluent cell layer was observed only in the Ti/IAPP+BMP-2 group (Fig. 6E). Moreover, only the Ti/IAPP+BMP-2 group was associated with a typical osteoblast-like cell morphology (i.e. enhanced cell spreading and flat cell body), whereas a spindle-like cell morphology was seen in the bare Ti and Ti+BMP-2 groups reminiscent of undifferentiated MSCs. To quantify changes in osteoblast differentiation, the ALP activity in MSCs was measured as an early marker of osteogenic differentiation. ALP is considered as one of the most important bone markers, since the induction *in vitro* predicts *in vivo* bone formation [74]. Both physisorbed and covalently immobilized BMP-2 significantly increased the ALP expression in MSCs, with the ALP induction being the highest in the Ti/IAPP group (Fig. 6F). To better resemble the *in vivo* environment, where biomolecule removal by chemical means is more likely to occur [22], the implants were subjected to detergent washing using Tween. This detergent wash-

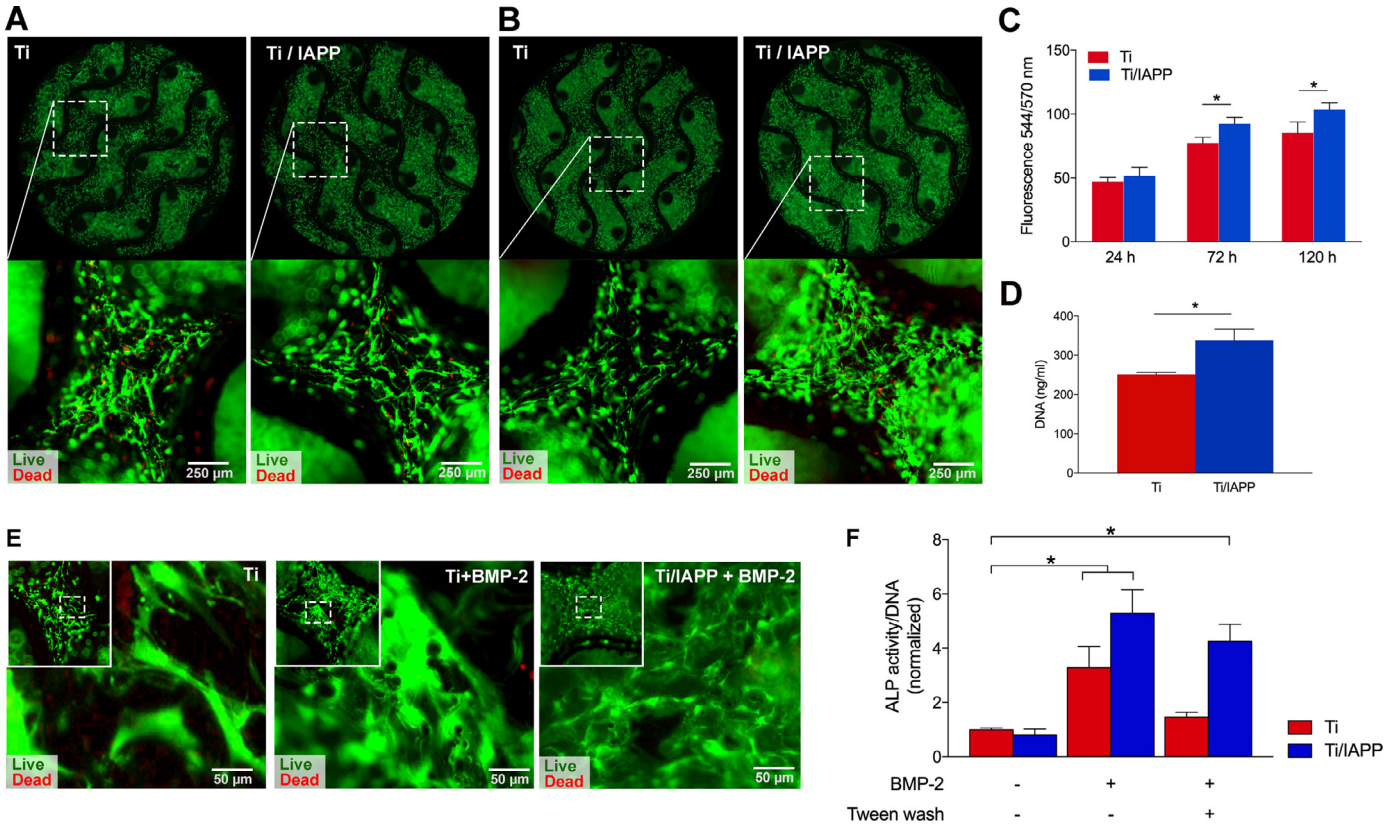

Fig. 6. Human MSC cytocompatibility and osteoblast differentiation. (a, b) Calcein/ethidium homodimer staining performed after 24 h (a) or 120 h (b) culture of MSCs on untreated and IAPP-functionalization implants. (c) Metabolic activity of MSCs cultured on untreated or IAPP-functionalized implants as measured by the Alamar Blue assay. (d) DNA content measured after 5-day MSC culture on untreated or IAPP-functionalization implants. (e) Calcein/ethidium homodimer staining showing the MSC cell morphology after 5 days culture on untreated or BMP-2 immobilized (15 µg/ml) Ti and Ti/IAPP implants. (f) ALP/DNA quantification in MSCs cultured for 5 days on bare Ti or IAPP-coated surfaces, with and without BMP-2 immobilization (15 µg/ml). Samples were either or not washed with 5% Tween-20 prior to cell seeding to remove non-covalent protein interactions. Data represent the mean ± SD ($n = 5$). $^*p < 0.05$ (one-way ANOVA).

ing resulted in a loss of the physisorbed BMP-2, whereas BMP-2 bioactivity remained largely intact due to the covalent attachment on the Ti/IAPP implants (Fig. 6F).

The results shown in Figs. 5 and 6 provide evidence that the IPP films render the implants with a more stable pro-osteogenic coating due to its elution-resistant nature, as opposed to the physically-adsorbed proteins on the bare Ti implants. Importantly, BMP-2 retained its bioactivity after its covalent attachment, as shown by the ALP induction in ATDC5 cells and MSCs following detergent washing. Moreover, the level of ALP induction was equal to that observed for physically-adsorbed BMP-2 prior to detergent washing. The importance of different routes of BMP signal transduction is still under debate. In particular, the role of ligand-receptor internalization and recycling of the formed complex has not been clarified [75,76]. It has been suggested that ligand-receptor interaction at the cell membrane, and subsequent formation of active heterodimeric complexes was the predominant mechanism of sustained MSC osteogenic stimulation by IAPP/BMP-2 functionalized implants [77]. In addition, the mildly hydrophilic character of the IAPP films (water contact angle of ~ 59° measured on a 2D Ti surface) [34] is beneficial for protein immobilization, as it prevents protein denaturation and interferes less with the protein conformation as compared to hydrophobic surfaces [76,78].

3.7. In vivo *study*

Although a foreign body response (FBR) will occur in response to all biomaterials at least to some extent, an unwanted FBR towards a biomaterial is characterized by excessive inflammation, giant cell fusion, and fibrous capsule formation at the material-tissue interface [79]. An excessive FBR *in vivo* of the developed implants is highly unwanted, as it negatively influences their rigid fixation and long-term osseointegration [80]. *In vitro*, it was first shown that the IAPP films supported the adhesion and viability of macrophages (Fig. 7A), without promoting undesirable NF-κB activation (Fig. 7B). This is an important finding, since chronic NF-κB activation around Ti implants contributes to osteoclast differentiation via RANK/RANKL signaling, which increases bone destruction and reduces bone formation [81].

The cytocompatibility of the IAPP films was confirmed *in vivo*. Following eight-week subcutaneous implantation, vascularized connective tissue ingrowth was seen in all groups without signs of FBR or excessive acute/chronic inflammation such as foreign body giant cell formation of fibrous encapsulation directly around the implant, irrespective of IAPP and/or BMP-2 coating (Fig. 8A). This indicates that, despite the high concentrations of radicals embedded within the structure, the IAPP films did not induce a specific protein adsorption or host activation leading to an unwanted inflammatory response [82]. This biocompatibility of the IAPP interlayer is an important advantage over other immobilization or drug delivery systems. For example, commonly-used polymeric delivery systems or their degradation products can negatively modulate the osteogenic or immune response [83,84], or can create an additional surface for bacterial adherence and immune evasion [84]. Moreover, one could speculate that the minimal usage of chemicals and reagents in the IAPP process is particularly attractive for gaining regulatory approvals.

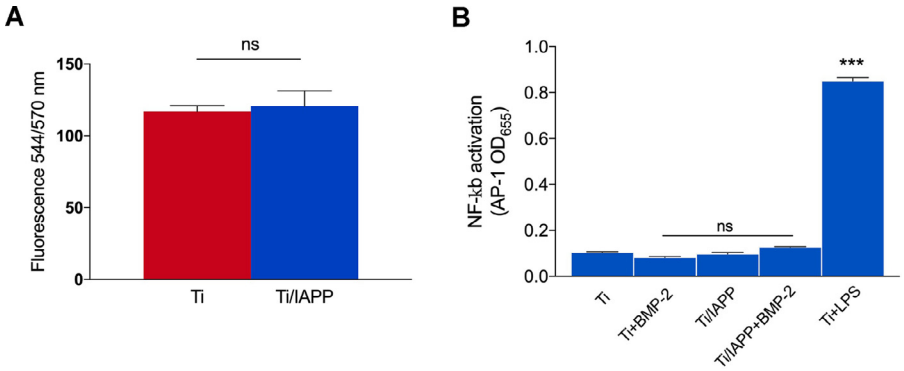

Fig. 7. Macrophage cytocompatibility and pro-inflammatory activity of IAPP films. (a) 24 h metabolic activity as measured by the Alamar Blue assay in RAW-Blue macrophages cultured on bare Ti and IAPP-functionalized implants. (b) NF-κB activation in RAW-Blue macrophages cultured for 24 h on different functionalized implants. LPS-preincubated Ti implants were used as a positive control for NF-κB activation. Data represent the mean ± SD ($n = 3$). $^{***}p < 0.0005$ (Mann-Whitney U).

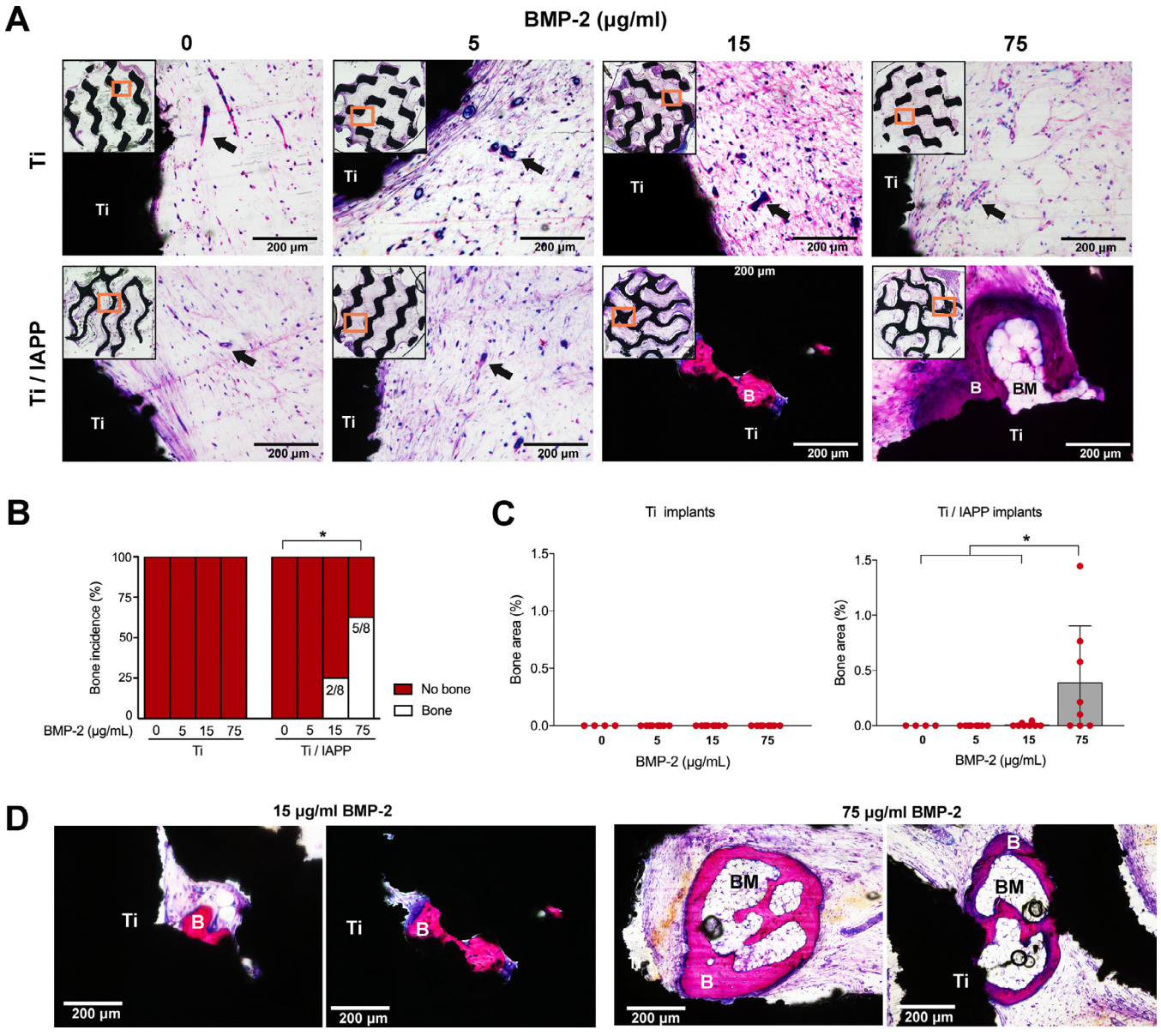

Fig. 8. *In vivo* bone induction. (a) Histological sections stained with methylene blue and basic fuchsin showing new bone tissue in bright pink after 8 weeks subcutaneous implantation in rats. The arrows indicate blood vessels. The images are representative for the group. (b, c) Bone formation was quantified in terms of the bone incidence (b) and bone volume (c). (d) Histological images showing the bone microenvironment in the Ti/IAPP groups. The images are taken from two different donors and are representative for the group. B: bone, BM: bone marrow, Ti: titanium. Data represent the mean ± SD (groups without BMP-2: $n = 4$, groups with BMP-2: $n = 8$). $^{*}p < 0.05$ (b: Linear mixed-model approach, c: one-way ANOVA) (For interpretation of the references to color in this figure, the reader is referred to the web version of this article.)

BMPs are unique proteins in terms of their osteoinductive behavior [85], which can also be evaluated on the functionalized implants in the subcutaneous implantation model. As a prerequisite for osseointegration, new bone formation in this model relies on the recruitment and differentiation of osteoprogenitor cells towards mature osteoblasts [17,86]. The current subcutaneous study therefore served as proof-of-principle to study solely the osteoinductive effects of the implants mediated by BMP-2, prior to moving on to functional bone healing models (e.g. bone defects, spinal fusion). As a main finding, only IAPP functionalized implants loaded with BMP-2 were capable of inducing new bone formation (Fig. 8A). Furthermore, there was a significant association ($p = 0.003$) between the amount of BMP-2 applied in the coating and the incidence of bone formation (Fig. 8B). The amount of bone was also significantly highest in the group with the highest BMP-2 load (Fig. 8C). New bone formation mainly occurred in protective areas of the implants, such as in micropores, concavities, or between Ti struts within closest proximity (Fig. 8D), showing the importance of the implant geometry in the observed bone induction. Even though the porosity and geometry of the current metallic implants were optimized to resemble native bone [39], the subcutaneous implantation model clearly demonstrated the superiority of the IAPP/BMP-2 coating in bone induction. Considering that the subcutaneous model carries the minimal presence of osteogenic cells [17,72], nor the mechanical loads that contribute to BMP-2 signaling pathways [87], it is hypothesized that the osteogenic performance of the coated implants would be even better appreciated in bone defect models compatible with the current porous biomaterials (i.e. segmental bone defect and spinal fusion models) [88,89].

These results show that the bone-inductive effect of BMP-2 is enhanced after covalent attachment to porous titanium implants. The rapid wash out of BMP-2 [71] and its short half-life (1–4 h) *in vivo* [27] are presumed to be the reason why the clinically-required dose of BMP-2 (1–2 mg/carrier) [90] far exceeds the physiological BMP-2 concentration (in the order of ng/g bone) [91]. The *in vitro* and *in vivo* data support that IAPP-mediated covalent immobilization can better retain BMP-2 at the implant surface as compared to physisorbed BMP-2. Although there is no consensus about the optimal *in vivo* release profile for BMP-2, a burst release of BMP-2 generally leads to more bone formation in direct comparison to sustained delivery systems [71,92,93], With this respect, the IAPP covalent immobilization method maximizes the amount of BMP-2 at the implant surface without hampering its immediate exposure to surrounding target cells, providing the initial stimulus needed for the onset of bone formation. Off-target effects, including uncontrolled bone formation, neurological deficits, tissue swelling, of BMP-2 are particularly worrisome in high-risk sites such as the cervical spine [29], leading to a statement by the FDA to avoid BMP (Infuse®) for this specific indication in 2008 [94]. In 2015, the approval of BMP-2 product (InductOs®) was even withdrawn in Europe [29]. For such high-risk indications, IAPP functionalized porous titanium could offer an improved safety profile and minimize the risk of undesirable effects at locations beyond the implant site.

The current IAPP-functionalized porous titanium can be considered as a versatile platform technology for the fabrication of various bio-functionalized orthopedic implants. Multifunctional approaches are of interest, since the delivery of a single protein may be a too simplistic approach to recapitulate the physiological bone healing process [95]. In particular, novel implants should be able to modulate the local immune response to favor osteogenesis and implant osseointegration. For example, a combinatorial coating with pro-inflammatory cytokines can likely improve the efficacy of osteoinductive proteins [45,46,96]. Covalent attachment of antimicrobial compounds onto porous metallic implants could furthermore prolong their bactericidal properties and better protect them from infectious loosening, which should be considered as another crucial bio-functionality. With this respect, the covalent immobilization of antibacterial agents on Ti implant surface has been explored as an effective strategy to prevent local colonization of bacteria and thereby biofilm formation [97]. These surfaces are permanently stable and release the conjugated antibacterial agents once their bonding is broken mechanically or chemically [98]. Of note, IAPP-based functionalization alone may not always be sufficient. For infection prevention, tunable release strategies may be required in addition to create a larger protective zone and provide active support against pre-operative, hematogenous, or contiguous infection [4,99,100]. In the same line of reasoning, covalent immobilization alone may be undesirable for biomolecules that require a chemical concentration gradient to be established, such as chemotactic cytokines for cell trafficking to the implant [101,102].

4. Conclusions

We proposed the one-step coating of porous titanium implants with an ion-assisted plasma polymer (IAPP) interlayer to create bio-functionalized load-bearing implants. We demonstrated that IAPP functionalization of additively-manufactured Ti implants significantly enhances their bone-inductive performance, which is explained by the higher density and stability of the reactive IAPP layer as compared to traditional plasma polymer films. The IAPP layer allows for firm anchorage of the biomolecules without constraining their bioactivity via reaction with reactive radicals embedded in it. For improved clinical translation, virtually any biomolecule can be attached without the use of coupling agents. The proven compatibility of AM and IAPP technologies provides a platform for the design of bioactive bone-mimicking implants. The long-term performance of such implants should next be investigated in relevant bone implantation models.

Declaration of Competing Interest

The authors declare that they have no known competing financial interests or personal relationships that could have appeared to influence the work reported in this paper.

Acknowledgements

The research for this paper was financially supported by the University of Sydney – Utrecht University Partnership Collaboration Award (grant no. CB.842300.3.50.029) and by the Australian Research Council (ARC).

Data availability

The authors declare that all data supporting the findings of this study are available within the article or from the corresponding author upon reasonable request.

References

[1] B.M. Holzapfel, J.C. Reichert, J.-T. Schantz, U. Gbureck, L. Rackwitz, U. Nöth, F. Jakob, M. Rudert, J. Groll, D.W. Hutmacher, How smart do biomaterials need to be? A translational science and clinical point of view, Adv. Drug Deliv. Rev. 65 (4) (2013) 581–603.
[2] M. Navarro, A. Michiardi, O. Castano, J.A. Planell, Biomaterials in orthopaedics, J R Soc. Interface 5 (27) (2008) 1137–1158.
[3] C.P. Bechtel, J.J. Gebhart, J.M. Tatro, E. Kiss-Toth, J.M. Wilkinson, E.M. Greenfield, Particle-induced osteolysis is mediated by TIRAP/Mal *in vitro* and *in vivo*: dependence on adherent pathogen-associated molecular patterns, JBJS 98 (4) (2016) 285–294.
[4] J. Raphel, M. Holodniy, S.B. Goodman, S.C. Heilshorn, Multifunctional coatings to simultaneously promote osseointegration and prevent infection of orthopaedic implants, Biomaterials 84 (2016) 301–314.

[5] K.J. Bozic, S.M. Kurtz, E. Lau, K. Ong, V. Chiu, T.P. Vail, H.E. Rubash, D.J. Berry, The epidemiology of revision total knee arthroplasty in the United States, Clinical Orthopaed. Related Res. 468 (1) (2010) 45–51.

[6] P.H. Wooley, E.M. Schwarz, Aseptic loosening, Gene Therapy 11(4) (2004) 402–407.

[7] C. Lavernia, D.J. Lee, V.H. Hernandez, The increasing financial burden of knee revision surgery in the United States, Clin. Orthop. Relat. Res. 446 (2006) 221–226.

[8] S. Amin Yavari, J. van der Stok, Y.C. Chai, R. Wauthle, Z.T. Birgani, P. Habibovic, M. Mulier, J. Schrooten, H. Weinans, A.A. Zadpoor, Bone regeneration performance of surface-treated porous titanium, Biomaterials 35 (24) (2014) 6172–6181.

[9] A.A. Zadpoor, Additively manufactured porous metallic biomaterials, J. Mater. Chem. B 7 (26) (2019) 4088–4117.

[10] S. Amin Yavari, S.M. Ahmadi, R. Wauthle, B. Pouran, J. Schrooten, H. Weinans, A.A. Zadpoor, Relationship between unit cell type and porosity and the fatigue behavior of selective laser melted meta-biomaterials, J. Mech. Behav. Biomed. Mater 43 (2015) 91–100.

[11] F. Bobbert, K. Lietaert, A.A. Eftekhari, B. Pouran, S. Ahmadi, H. Weinans, A. Zadpoor, Additively manufactured metallic porous biomaterials based on minimal surfaces: a unique combination of topological, mechanical, and mass transport properties, Acta Biomater. 53 (2017) 572–584.

[12] H.M. Kolken, S. Janbaz, S.M. Leeflang, K. Lietaert, H.H. Weinans, A.A. Zadpoor, Rationally designed meta-implants: a combination of auxetic and conventional meta-biomaterials, Mater Horiz. 5 (1) (2018) 28–35.

[13] A.A. Zadpoor, Mechanical performance of additively manufactured meta-biomaterials, Acta Biomater 85 (2019) 41–59.

[14] S.A. Yavari, Y.C. Chai, A.J. Böttger, R. Wauthle, J. Schrooten, H. Weinans, A.A. Zadpoor, Effects of anodizing parameters and heat treatment on nanotopographical features, bioactivity, and cell culture response of additively manufactured porous titanium, Mater. Sci. Eng. C 51 (2015) 132–138.

[15] S. Amin Yavari, J. van der Stok, S.M. Ahmadi, R. Wauthle, J. Schrooten, H. Weinans, A.A. Zadpoor, Mechanical analysis of a rodent segmental bone defect model: the effects of internal fixation and implant stiffness on load transfer, J. Biomech. 47 (11) (2014) 2700–2708.

[16] L. Tayebi, M. Rasoulianboroujeni, K. Moharamzadeh, T.K.D. Almela, Z. Cui, H. Ye, 3D-printed membrane for guided tissue regeneration, Mater. Sci. Eng. C 84 (2018) 148–158.

[17] T. Albrektsson, C Johansson, Osteoinduction, osteoconduction and osseointegration, Eur. Spine J. 10 (Suppl 2) (2001) S96–101.

[18] A. Gristina, Biomaterial-centered infection: microbial adhesion versus tissue integration, Science 237 (4822) (1987) 1588–1595.

[19] S. Bakhshandeh, Z. Gorgin Karaji, K. Lietaert, A.C. Fluit, C.E. Boel, H.C. Vogely, T. Vermonden, W.E. Hennink, H. Weinans, A.A. Zadpoor, S. Amin Yavari, Simultaneous Delivery of Multiple Antibacterial Agents from Additively Manufactured Porous Biomaterials to Fully Eradicate Planktonic and Adherent Staphylococcus aureus, ACS Appl. Mater Interf. 9 (31) (2017) 25691–25699.

[20] C. Stewart, B. Akhavan, S.G. Wise, M.M. Bilek, A review of biomimetic surface functionalization for bone-integrating orthopedic implants: mechanisms, current approaches, and future directions, Prog. Mater. Sci. (2019) 100588.

[21] S. Bakhshandeh, S.A. Yavari, Electrophoretic deposition: a versatile tool against biomaterial associated infections, J. Mater. Chem. B 6 (8) (2018) 1128–1148.

[22] L. Vroman, Effect of absorbed proteins on the wettability of hydrophilic and hydrophobic solids, Nature 196 (1962) 476–477.

[23] V. Hlady, J. Buijs, Protein adsorption on solid surfaces, Curr. Opin. Biotechnol. 7 (1) (1996) 72–77.

[24] W. Norde, A.C. Anusiem, Adsorption, desorption and re-adsorption of proteins on solid surfaces, Colloids Surfaces 66 (1) (1992) 73–80.

[25] R. Fu, S. Selph, M. McDonagh, K. Peterson, A. Tiwari, R. Chou, M. Helfand, Effectiveness and harms of recombinant human bone morphogenetic protein-2 in spine fusion: a systematic review and meta-analysis, Ann. Intern Med. 158 (12) (2013) 890–902.

[26] K.R. Garrison, S. Donell, J. Ryder, I. Shemilt, M. Mugford, I. Harvey, F. Song, Clinical effectiveness and cost-effectiveness of bone morphogenetic proteins in the non-healing of fractures and spinal fusion: a systematic review, Health Technol. Assess 11 (30) (2007) 1–150 iii-iv.

[27] S. Suliman, Z. Xing, X. Wu, Y. Xue, T.O. Pedersen, Y. Sun, A.P. Doskeland, J. Nickel, T. Waag, H. Lygre, A. Finne-Wistrand, D. Steinmuller-Nethl, A. Krueger, K. Mustafa, Release and bioactivity of bone morphogenetic protein-2 are affected by scaffold binding techniques *in vitro* and *in vivo*, J. Control Release 197 (2015) 148–157.

[28] K. Schmidt-Bleek, B.M. Willie, P. Schwabe, P. Seemann, G.N. Duda, BMPs in bone regeneration: less is more effective, a paradigm-shift, Cytokine Growth Factor Rev. 27 (2016) 141–148.

[29] C.A. Tannoury, H.S. An, Complications with the use of bone morphogenetic protein 2 (BMP-2) in spine surgery, Spine J. 14 (3) (2014) 552–559.

[30] H. Yuk, T. Zhang, G.A. Parada, X. Liu, X. Zhao, Skin-inspired hydrogel–elastomer hybrids with robust interfaces and functional microstructures, Nat. Commun. 7 (2016) 12028.

[31] S.E. Kim, C.S. Kim, Y.P. Yun, D.H. Yang, K. Park, S.E. Kim, C.M. Jeong, J.B. Huh, Improving osteoblast functions and bone formation upon BMP-2 immobilization on titanium modified with heparin, Carbohydr. Polym. 114 (2014) 123–132.

[32] B. Akhavan, K. Jarvis, P. Majewski, Hydrophobic plasma polymer coated silica particles for petroleum hydrocarbon removal, ACS Appl. Mater Interf. 5 (17) (2013) 8563–8571.

[33] B. Akhavan, T.D. Michl, C. Giles, K. Ho, L. Martin, O. Sharifahmadian, S.G. Wise, B.R. Coad, N. Kumar, H.J. Griesser, Plasma activated coatings with dual action against fungi and bacteria, Appl. Mater. 12 (2018) 72–84 Today.

[34] L.J. Martin, B. Akhavan, M.M. Bilek, Electric fields control the orientation of peptides irreversibly immobilized on radical-functionalized surfaces, Nat. Commun. 9 (1) (2018) 357.

[35] B. Akhavan, M. Croes, S.G. Wise, C. Zhai, J. Hung, C. Stewart, M. Ionescu, H. Weinans, Y. Gan, S.A. Yavari, Radical-functionalized plasma polymers: stable biomimetic interfaces for bone implant applications, Appl. Mater. Today 16 (2019) 456–473.

[36] C.A. Stewart, B. Akhavan, M. Santos, J. Hung, C.L. Hawkins, B. Bao, S.G. Wise, M.M. Bilek, Cellular responses to radical propagation from ion-implanted plasma polymer surfaces, Appl. Surf. Sci. 456 (2018) 701–710.

[37] M.M.M. Bilek, D.V. Bax, A. Kondyurin, Y.B. Yin, N.J. Nosworthy, K. Fisher, A. Waterhouse, A.S. Weiss, C.G. dos Remedios, D.R. McKenzie, Free radical functionalization of surfaces to prevent adverse responses to biomedical devices, Proc. Natl. Acad. Sci. U. S. A. 108 (35) (2011) 14405–14410.

[38] C.A. Stewart, B. Akhavan, J. Hung, S. Bao, J.-.H. Jang, S.G. Wise, M.M. Bilek, Multifunctional protein-immobilized plasma polymer films for orthopedic applications, ACS Biomater. Sci. Eng. 4 (12) (2018) 4084–4094.

[39] H. Jinnai, Y. Nishikawa, M. Ito, S.D. Smith, D.A. Agard, R.J. Spontak, Topological similarity of sponge-like bicontinuous morphologies differing in length scale, Adv. Mater. 14 (22) (2002) 1615–1618.

[40] J. Schindelin, I. Arganda-Carreras, E. Frise, V. Kaynig, M. Longair, T. Pietzsch, S. Preibisch, C. Rueden, S. Saalfeld, B. Schmid, J.Y. Tinevez, D.J. White, V. Hartenstein, K. Eliceiri, P. Tomancak, A. Cardona, Fiji: an open-source platform for biological-image analysis, Nat Methods 9 (7) (2012) 676–682.

[41] I. 13314:2011, Mechanical testing of metals — Ductility testing — Compression test for porous and cellular metals, 2019.

[42] B. Akhavan, S.G. Wise, M.M.M. Bilek, Substrate-Regulated growth of plasma-polymerized films on carbide-forming metals, Langmuir 32 (42) (2016) 10835–10843.

[43] L.D. Loozen, A. Vandersteen, A.H. Kragten, F.C. Oner, W.J. Dhert, M.C. Kruyt, J. Alblas, Bone formation by heterodimers through non-viral gene delivery of BMP-2/6 and BMP-2/7, Eur. Cell Mater 35 (2018) 195–208.

[44] A.M. Kandahari, X. Yang, K.A. Laroche, A.S. Dighe, D. Pan, Q. Cui, A review of UHMWPE wear-induced osteolysis: the role for early detection of the immune response, Bone. Res. 4 (2016) 16014.

[45] M. Croes, F.C. Oner, D. van Neerven, E. Sabir, M.C. Kruyt, T.J. Blokhuis, W.J.A. Dhert, J. Alblas, Proinflammatory T cells and IL-17 stimulate osteoblast differentiation, Bone 84 (2016) 262–270.

[46] M. Croes, M.C. Kruyt, W.M. Groen, K.M.A. van Dorenmalen, W.J.A. Dhert, F.C. Oner, J. Alblas, Interleukin 17 enhances bone morphogenetic protein-2-induced ectopic bone formation, Sci. Rep. 8 (1) (2018) 7269.

[47] D.H. Wiznia, R. Schwarzkopf, R. Iorio, W.J. Long, Factors That Influence Bone-Ingrowth Fixation of Press-Fit Acetabular Cups, JBJS Rev. 7 (6) (2019) e2.

[48] H. Jinnai, H. Watashiba, T. Kajihara, Y. Nishikawa, M. Takahashi, M. Ito, Surface curvatures of trabecular bone microarchitecture, Bone 30 (1) (2002) 191–194.

[49] Z. Gorgin Karaji, M. Speirs, S. Dadbakhsh, J.-.P. Kruth, H. Weinans, A. Zadpoor, S. Amin Yavari, Additively manufactured and surface biofunctionalized porous nitinol, ACS Appl. Mater Interf. 9 (2) (2017) 1293–1304.

[50] H.W. Keaveny TM, Mechanical properties of cortical and trabecular bone, in: H. BK (Ed.), Bone Mechanics Handbooks, 7, CRC Press, Boca RatonFL, 1993, pp. 285–344.

[51] V. Karageorgiou, D. Kaplan, Porosity of 3D biomaterial scaffolds and osteogenesis, Biomaterials 26 (27) (2005) 5474–5491.

[52] L. Yang, C. Yan, H. Fan, Z. Li, C. Cai, P. Chen, Y. Shi, S. Yang, Investigation on the orientation dependence of elastic response in Gyroid cellular structures, J. Mech. Behav. Biomed. Mater 90 (2019) 73–85.

[53] M. Smith, Z. Guan, W. Cantwell, Finite element modelling of the compressive response of lattice structures manufactured using the selective laser melting technique, Int. J. Mech. Sci. 67 (2013) 28–41.

[54] L. Yang, C. Yan, W. Cao, Z. Liu, B. Song, S. Wen, C. Zhang, Y. Shi, S. Yang, Compression–compression fatigue behaviour of gyroid-type triply periodic minimal surface porous structures fabricated by selective laser melting, Acta Mater. 181 (2019) 49–66.

[55] A. Ataee, Y. Li, M. Brandt, C. Wen, Ultrahigh-strength titanium gyroid scaffolds manufactured by selective laser melting (SLM) for bone implant applications, Acta Mater. 158 (2018) 354–368.

[56] C. Han, Y. Li, Q. Wang, S. Wen, Q. Wei, C. Yan, L. Hao, J. Liu, Y. Shi, Continuous functionally graded porous titanium scaffolds manufactured by selective laser melting for bone implants, J. Mech. Behav. Biomed. Mater 80 (2018) 119–127.

[57] R.B. B.D.B. Martin, N.A. Sharkey, D.P. Fyhrie, Mechanical Properties of Bone, Skeletal Tissue Mechanics, Springer, 2015, pp. 355–422.

[58] S.B. Goodman, The effects of micromotion and particulate materials on tissue differentiation. Bone chamber studies in rabbits, Acta Orthop. Scand Suppl. 258 (1994) 1–43.

[59] R.A. Berger, J.J. Jacobs, R.M. Meneghini, C. Della Valle, W. Paprosky, A.G. Rosenberg, Rapid rehabilitation and recovery with minimally invasive total hip arthroplasty, Clin. Orthop. Relat. Res. (429) (2004) 239–247.

[60] M. Esposito, M.G. Grusovin, H. Maghaireh, H.V. Worthington, Interventions for replacing missing teeth: different times for loading dental implants, Cochrane Database Syst. Rev. (3) (2013) CD003878.
[61] A. Mombelli, N. Cionca, Systemic diseases affecting osseointegration therapy, Clin. Oral. Implants Res. 17 (Suppl 2) (2006) 97–103.
[62] B. Akhavan, K. Jarvis, P. Majewski, Development of negatively charged particulate surfaces through a dry plasma-assisted approach, RSC Adv. 5 (17) (2015) 12910–12921.
[63] F. Khelifa, S. Ershov, Y. Habibi, R. Snyders, P. Dubois, Free-radical-induced grafting from plasma polymer surfaces, Chem. Rev. 116 (6) (2016) 3975–4005.
[64] P. Rupper, M. Vandenbossche, L. Bernard, D. Hegemann, M. Heuberger, Composition and stability of plasma polymer films exhibiting vertical chemical gradients, Langmuir 33 (9) (2017) 2340–2352.
[65] J. Robertson, Diamond-like amorphous carbon, Mater. Sci. Eng. R-Rep. 37 (4–6) (2002) 129–281.
[66] B. Akhavan, B. Menges, R. Förch, Inhomogeneous Growth of Micrometer Thick Plasma Polymerized Films, Langmuir 32 (19) (2016) 4792–4799.
[67] A. Gopferich, Mechanisms of polymer degradation and erosion, Biomaterials 17 (2) (1996) 103–114.
[68] M. Feng, A.B. Morales, A. Poot, T. Beugeling, A. Bantjes, Effects of Tween 20 on the desorption of proteins from polymer surfaces, J. Biomater Sci. Polym. Ed. 7 (5) (1995) 415–424.
[69] E.T. Vandenberg, U.J. Krull, The prevention of adsorption of interferents to radiolabelled protein by Tween 20, J. Biochem. Biophys. Methods 22 (4) (1991) 269–277.
[70] K. Kashiwagi, T. Tsuji, K. Shiba, Directional BMP-2 for functionalization of titanium surfaces, Biomaterials 30 (6) (2009) 1166–1175.
[71] D.H. Kempen, L. Lu, T.E. Hefferan, L.B. Creemers, A. Maran, K.L. Classic, W.J. Dhert, M.J. Yaszemski, Retention of *in vitro* and *in vivo* BMP-2 bioactivities in sustained delivery vehicles for bone tissue engineering, Biomaterials 29 (22) (2008) 3245–3252.
[72] J.E. Davies, Bone bonding at natural and biomaterial surfaces, Biomaterials 28 (34) (2007) 5058–5067.
[73] S. Zwingenberger, Z. Yao, A. Jacobi, C. Vater, R.D. Valladares, C. Li, C. Nich, A.J. Rao, J.E. Christman, J.K. Antonios, E. Gibon, A. Schambach, T. Maetzig, S.B. Goodman, M. Stiehler, Enhancement of BMP-2 induced bone regeneration by SDF-1alpha mediated stem cell recruitment, Tissue Eng. Part A 20 (3–4) (2014) 810–818.
[74] H.J. Prins, A.K. Braat, D. Gawlitta, W.J. Dhert, D.A. Egan, E. Tijssen-Slump, H. Yuan, P.J. Coffer, H. Rozemuller, A.C. Martens, *In vitro* induction of alkaline phosphatase levels predicts *in vivo* bone forming capacity of human bone marrow stromal cells, Stem Cell Res. 12 (2) (2014) 428–440.
[75] G.M. Di Guglielmo, C. Le Roy, A.F. Goodfellow, J.L. Wrana, Distinct endocytic pathways regulate TGF-beta receptor signalling and turnover, Nat .Cell Biol. 5 (5) (2003) 410–421.
[76] R.J. Gleason, A.M. Akintobi, B.D. Grant, R.W. Padgett, BMP signaling requires retromer-dependent recycling of the type I receptor, Proc. Natl. Acad. Sci. U S A 111 (7) (2014) 2578–2583.
[77] E.H. Schwab, T.L. Pohl, T. Haraszti, G.K. Schwaerzer, C. Hiepen, J.P. Spatz, P. Knaus, E.A. Cavalcanti-Adam, Nanoscale control of surface immobilized BMP-2: toward a quantitative assessment of BMP-mediated signaling events, Nano Lett. 15 (3) (2015) 1526–1534.
[78] R. Olivares-Navarrete, P. Raz, G. Zhao, J. Chen, M. Wieland, D.L. Cochran, R.A. Chaudhri, A. Ornoy, B.D. Boyan, Z. Schwartz, Integrin alpha2beta1 plays a critical role in osteoblast response to micron-scale surface structure and surface energy of titanium substrates, Proc. Natl. Acad. Sci. USA 105 (41) (2008) 15767–15772.
[79] J.M. Anderson, A. Rodriguez, D.T. Chang, Foreign Body Reaction to biomaterials, Seminars in Immunology, Elsevier, 2008, pp. 86–100.
[80] S. Spriano, S. Yamaguchi, F. Baino, S. Ferraris, A critical review of multifunctional titanium surfaces: new frontiers for improving osseointegration and host response, avoiding bacteria contamination, Acta Biomater 79 (2018) 1–22.
[81] T.H. Lin, Y. Tamaki, J. Pajarinen, H.A. Waters, D.K. Woo, Z. Yao, S.B. Goodman, Chronic inflammation in biomaterial-induced periprosthetic osteolysis: nF-kappaB as a therapeutic target, Acta Biomater 10 (1) (2014) 1–10.
[82] S. Franz, S. Rammelt, D. Scharnweber, J.C. Simon, Immune responses to implants - a review of the implications for the design of immunomodulatory biomaterials, Biomaterials 32 (28) (2011) 6692–6709.
[83] D. Barbieri, H. Yuan, F. de Groot, W.R. Walsh, J.D. de Bruijn, Influence of different polymeric gels on the ectopic bone forming ability of an osteoinductive biphasic calcium phosphate ceramic, Acta Biomater 7 (5) (2011) 2007–2014.
[84] M. Croes, S. Bakhshandeh, I.A.J. van Hengel, K. Lietaert, K.P.M. van Kessel, B. Pouran, B.C.H. van der Wal, H.C. Vogely, W. Van Hecke, A.C. Fluit, C.H.E. Boel, J. Alblas, A.A. Zadpoor, H. Weinans, S. Amin Yavari, Antibacterial and immunogenic behavior of silver coatings on additively manufactured porous titanium, Acta Biomater 81 (2018) 315–327.
[85] A.H. Reddi, BMPs: from bone morphogenetic proteins to body morphogenetic proteins, Cytokine Growth Factor Rev. 16 (3) (2005) 249–250.
[86] D.R. Lemos, C. Eisner, C.I. Hopkins, F.M.V. Rossi, Skeletal muscle-resident MSCs and bone formation, Bone 80 (2015) 19–23.
[87] C. Schwarz, D. Wulsten, A. Ellinghaus, J. Lienau, B.M. Willie, G.N. Duda, Mechanical load modulates the stimulatory effect of BMP2 in a rat nonunion model, Tissue Eng. Part A 19 (1–2) (2013) 247–254.
[88] F. Kandziora, G. Schollmeier, M. Scholz, J. Schaefer, A. Scholz, G. Schmidmaier, R. Schroder, H. Bail, G. Duda, T. Mittlmeier, N.P. Haas, Influence of cage design on interbody fusion in a sheep cervical spine model, J. Neurosurg. 96 (3 Suppl) (2002) 321–332.
[89] J. van der Stok, M.K. Koolen, M.P. de Maat, S. Amin Yavari, J. Alblas, P. Patka, J.A. Verhaar, E.M. van Lieshout, A.A. Zadpoor, H. Weinans, H. Jahr, Full regeneration of segmental bone defects using porous titanium implants loaded with BMP-2 containing fibrin gels, Eur. Cell Mater 29 (2015) 141–153 discussion 153-4.
[90] S. Govender, C. Csimma, H.K. Genant, A. Valentin-Opran, Y. Amit, R. Arbel, H. Aro, D. Atar, M. Bishay, M.G. Borner, P. Chiron, P. Choong, J. Cinats, B. Courtenay, R. Feibel, B. Geulette, C. Gravel, N. Haas, M. Raschke, E. Hammacher, D. van der Velde, P. Hardy, M. Holt, C. Josten, R.L. Ketterl, B. Lindeque, G. Lob, H. Mathevon, G. McCoy, D. Marsh, R. Miller, E. Munting, S. Oevre, L. Nordsletten, A. Patel, A. Pohl, W. Rennie, P. Reynders, P.M. Rommens, J. Rondia, W.C. Rossouw, P.J. Daneel, S. Ruff, A. Ruter, S. Santavirta, T.A. Schildhauer, C. Gekle, R. Schnettler, D. Segal, H. Seiler, R.B. Snowdowne, J. Stapert, G. Taglang, R. Verdonk, L. Vogels, A. Weckbach, A. Wentzensen, T. Wisniewski, B.M.P.E.i.S.f.T.T.S. Group, Recombinant human bone morphogenetic protein-2 for treatment of open tibial fractures: a prospective, controlled, randomized study of four hundred and fifty patients, J. Bone Joint Surg. Am. 84 (12) (2002) 2123–2134.
[91] W.S. Pietrzak, J. Woodell-May, N. McDonald, Assay of bone morphogenetic protein-2, -4, and -7 in human demineralized bone matrix, J. Craniofac. Surg. 17 (1) (2006) 84–90.
[92] R.E. Geuze, L.F. Theyse, D.H. Kempen, H.A. Hazewinkel, H.Y. Kraak, F.C. Oner, W.J. Dhert, J. Alblas, A differential effect of bone morphogenetic protein-2 and vascular endothelial growth factor release timing on osteogenesis at ectopic and orthotopic sites in a large-animal model, Tissue Eng. Part A 18 (19–20) (2012) 2052–2062.
[93] M.G.L. Olthof, D.H.R. Kempen, X. Liu, M. Dadsetan, M.A. Tryfonidou, M.J. Yaszemski, W.J.A. Dhert, L. Lu, Bone morphogenetic protein-2 release profile modulates bone formation in phosphorylated hydrogel, J. Tissue Eng. Regen. Med. 12 (6) (2018) 1339–1351.
[94] E.P. Ramly, A.R. Alfonso, R.S. Kantar, M.M. Wang, J.R.D. Siso, A. Ibrahim, P.G. Coelho, R.L. Flores, Safety and Efficacy of Recombinant Human Bone Morphogenetic Protein-2 (rhBMP-2) in Craniofacial Surgery, Plastic Reconstruct. Surgery Global Open 7 (8) (2019) e2347.
[95] S. Amin Yavari, M. Croes, B. Akhavan, F. Jahanmard, C. Eigenhuis, S. Dadbakhsh, C. Vogely, M. Bilek, A. Fluit, E. Boel, B. van der Wal, T. Vermonden, H. Weinans, A. Zadpoor, Layer by layer coating for bio-functionalization of additively manufactured meta-biomaterials, Additive Manufact. (2020) 100991.
[96] M. Croes, M.C. Kruyt, W. Boot, B. Pouran, M.V. Braham, S.A. Pakpahan, H. Weinans, H.C. Vogely, A.C. Fluit, W.J. Dhert, J. Alblas, F.C. Oner, The role of bacterial stimuli in inflammation-driven bone formation, Eur. Cell Mater 37 (2019) 402–419.
[97] B. Akhavan, S. Bakhshandeh, H. Najafi-Ashtiani, A.C. Fluit, E. Boel, C. Vogely, B.C.H. van der Wal, A.A. Zadpoor, H. Weinans, W.E. Hennink, M.M. Bilek, S. Amin Yavari, Direct covalent attachment of silver nanoparticles on radical-rich plasma polymer films for antibacterial applications, J. Mater. Chem. B 6 (37) (2018) 5845–5853.
[98] V. Antoci, C.S. Adams, J. Parvizi, H.M. Davidson, R.J. Composto, T.A. Freeman, E. Wickstrom, P. Ducheyne, D. Jungkind, I.M. Shapiro, N.J. Hickok, The inhibition of Staphylococcus epidermidis biofilm formation by vancomycin-modified titanium alloy and implications for the treatment of periprosthetic infection, Biomaterials 29 (35) (2008) 4684–4690.
[99] A.I. Stavrakis, S. Zhu, V. Hegde, A.H. Loftin, A.G. Ashbaugh, J.A. Niska, L.S. Miller, T. Segura, N.M. Bernthal, *In vivo* Efficacy of a "Smart" Antimicrobial Implant Coating, J. Bone Joint Surg. Am. 98 (14) (2016) 1183–1189.
[100] H.J. Busscher, H.C. van der Mei, G. Subbiahdoss, P.C. Jutte, J.J. van den Dungen, S.A. Zaat, M.J. Schultz, D.W. Grainger, Biomaterial-associated infection: locating the finish line in the race for the surface, Sci. Transl. Med. 4 (153) (2012) 153rv10 153rv10.
[101] D.J. Ceradini, A.R. Kulkarni, M.J. Callaghan, O.M. Tepper, N. Bastidas, M.E. Kleinman, J.M. Capla, R.D. Galiano, J.P. Levine, G.C. Gurtner, Progenitor cell trafficking is regulated by hypoxic gradients through HIF-1 induction of SDF-1, Nat. Med. 10 (8) (2004) 858–864.
[102] E.L. Fong, C.K. Chan, S.B. Goodman, Stem cell homing in musculoskeletal injury, Biomaterials 32 (2) (2011) 395–409.